

## The ALMA-QUARKS Survey: Fibers' role in star formation unveiled in an intermediate-mass protocluster region of the Vela D cloud

DONGTING YANG,<sup>1</sup> HONG-LI LIU,<sup>1</sup> TIE LIU,<sup>2</sup> ANANDMAYEE TEJ,<sup>3</sup> XUNCHUAN LIU,<sup>2</sup> JINHUA HE,<sup>4</sup> GUIDO GARAY,<sup>5,6</sup> AMELIA STUTZ,<sup>7,8</sup> LEI ZHU,<sup>9</sup> SHENG-LI QIN,<sup>1</sup> FENGWEI XU,<sup>10,11</sup> PAK-SHING LI,<sup>2</sup> MIKA JUVELA,<sup>12</sup> PABLO GARCÍA,<sup>6,13</sup> PAUL F. GOLDSMITH,<sup>14</sup> SIJU ZHANG,<sup>15</sup> XINDI TANG,<sup>16</sup> PATRICIO SANHUEZA,<sup>17,18</sup> SHANGHUO LI,<sup>8</sup> CHANG WON LEE,<sup>19,20</sup> SWAGAT RANJAN DAS,<sup>5</sup> WENYU JIAO,<sup>2</sup> XIAOFENG MAI,<sup>21,22</sup> PRASANTA GORAI,<sup>23,24</sup> YICHEN ZHANG,<sup>25</sup> ZHIYUAN REN,<sup>26,27,28</sup> L. VIKTOR TÓTH,<sup>29</sup> JIHYE HWANG,<sup>19</sup> LEONARDO BRONFMAN,<sup>5</sup> KEN'ICHI TATEMATSU,<sup>18</sup> LOKESH DEWANGAN,<sup>30</sup> JAMES O. CHIBUEZE,<sup>31,32</sup> SUINAN ZHANG,<sup>2</sup> GANG WU,<sup>16</sup> AND JINJIN XIE<sup>2</sup>

<sup>1</sup>*School of physics and astronomy, Yunnan University, Kunming, 650091, PR China*

<sup>2</sup>*Shanghai Astronomical Observatory, Chinese Academy of Sciences, 80 Nandan Road, Shanghai 200030, Peoples Republic of China*

<sup>3</sup>*Indian Institute of Space Science and Technology, Thiruvananthapuram 695 547, Kerala, India*

<sup>4</sup>*Yunnan Observatories, Chinese Academy of Sciences, Kunming, 650216, Yunnan, PR China*

<sup>5</sup>*Departamento de Astronomía, Universidad de Chile, Casilla 36-D, Santiago, Chile*

<sup>6</sup>*Chinese Academy of Sciences South America Center for Astronomy, National Astronomical Observatories, CAS, Beijing 100101, China*

<sup>7</sup>*Departamento de Astronomía, Universidad de Concepción, Av. Esteban Iturra s/n, Distrito Universitario, 160-C, Chile*

<sup>8</sup>*Max Planck Institute for Astronomy, Königstuhl 17, D-69117 Heidelberg, Germany*

<sup>9</sup>*Chinese Academy of Sciences South America Center for Astronomy, National Astronomical Observatories, Chinese Academy of Sciences, Beijing, 100101, PR China*

<sup>10</sup>*Kavli Institute for Astronomy and Astrophysics, Peking University, 5 Yiheyuan Road, Haidian District, Beijing 100871, People's Republic of China*

<sup>11</sup>*Department of Astronomy, Peking University, 100871, Beijing, People's Republic of China*

<sup>12</sup>*Department of Physics, P.O. box 64, FI-00014, University of Helsinki, Finland*

<sup>13</sup>*Instituto de Astronomía, Universidad Católica del Norte, Av. Angamos 0610, Antofagasta, Chile*

<sup>14</sup>*Jet Propulsion Laboratory, California Institute of Technology, 4800 Oak Grove Drive, Pasadena, CA 91109, USA*

<sup>15</sup>*Departamento de Astronomía, Universidad de Chile, Las Condes, 7591245 Santiago, Chile*

<sup>16</sup>*Xinjiang Astronomical Observatory, Chinese Academy of Sciences, 150 Science 1-Street, Urumqi, Xinjiang 830011, People's Republic of China*

<sup>17</sup>*Department of Earth and Planetary Sciences, Tokyo Institute of Technology, Meguro, Tokyo, 152-8551, Japan*

<sup>18</sup>*National Astronomical Observatory of Japan, National Institutes of Natural Sciences, 2-21-1 Osawa, Mitaka, Tokyo 181-8588, Japan*

<sup>19</sup>*Korea Astronomy and Space Science Institute, 776 Daedeokdae-ro, Yuseong-gu, Daejeon 34055, Republic of Korea*

<sup>20</sup>*University of Science and Technology, Korea (UST), 217 Gajeong-ro, Yuseong-gu, Daejeon 34113, Republic of Korea*

<sup>21</sup>*Shanghai Astronomical Observatory, Chinese Academy of Sciences, Shanghai 200030, People's Republic of China*

<sup>22</sup>*School of Astronomy and Space Sciences, University of Chinese Academy of Sciences, No. 19A Yuquan Road, Beijing 100049, People's Republic of China*

<sup>23</sup>*Roseland Centre for Solar Physics, University of Oslo, PO Box 1029 Blindern, 0315 Oslo, Norway*

<sup>24</sup>*Institute of Theoretical Astrophysics, University of Oslo, PO Box 1029 Blindern, 0315 Oslo, Norway*

<sup>25</sup>*Department of Astronomy, Shanghai Jiao Tong University, 800 Dongchuan Rd., Minhang, Shanghai 200240, People's Republic of China*

<sup>26</sup>*National Astronomical Observatories, Chinese Academy of Sciences, Datun Road A20, Beijing, People's Republic of China*

<sup>27</sup>*CAS Key Laboratory of FAST, NAOC, Chinese Academy of Sciences, Beijing, China*

<sup>28</sup>*University of Chinese Academy of Sciences, Beijing, People's Republic of China*

<sup>29</sup>*Institute of Physics and Astronomy, Eötvös Loránd University, Pázmány Péter sétány 1/A, H-1117 Budapest, Hungary*

<sup>30</sup>*Physical Research Laboratory, Navrangpura, Ahmedabad—380 009, India*

Corresponding author: Hong-Li Liu

[hongliliu2012@gmail.com](mailto:hongliliu2012@gmail.com)

Corresponding author: Tie Liu

[liutie@shao.ac.cn](mailto:liutie@shao.ac.cn)

Corresponding author: Anandmayee Tej

[tej@iist.ac.in](mailto:tej@iist.ac.in)

Corresponding author: Xunchuan Liu

[liuxunchuan001@gmail.com](mailto:liuxunchuan001@gmail.com)

<sup>31</sup>*Department of Mathematical Sciences, University of South Africa, Cnr Christian de Wet Rd and Pioneer Avenue, Florida Park, 1709, Roodepoort, South Africa*

<sup>32</sup>*Department of Physics and Astronomy, Faculty of Physical Sciences, University of Nigeria, Carver Building, 1 University Road, Nsukka 410001, Nigeria*

(Received xxx; Revised xxx; Accepted xxx)

## ABSTRACT

In this paper, we present a detailed analysis of the IRS 17 filament within the intermediate-mass protocluster IRAS 08448-4343 (of  $\sim 10^3 L_\odot$ ), using ALMA data from the ATOMS 3-mm and QUARKS 1.3-mm surveys. The IRS 17 filament, which spans  $\sim 54000$  au (0.26 pc) in length and  $\sim 4000$  au (0.02 pc) in width, exhibits a complex, multi-component velocity field, and harbours hierarchical substructures. These substructures include three bundles of seven velocity-coherent fibers, and 29 dense ( $n \sim 10^8 \text{ cm}^{-3}$ ) condensations. The fibers have a median length of  $\sim 4500$  au and a median width of  $\sim 1400$  au. Among these fibers, four are identified as “fertile”, each hosting at least three dense condensations, which are regarded as the “seeds” of star formation. While the detected cores are randomly spaced within the IRS 17 filament based on the 3-mm dust continuum image, periodic spacing ( $\sim 1600$  au) of condensations is observed in the fertile fibers according to the 1.3-mm dust map, consistent with the predictions of linear isothermal cylinder fragmentation models. These findings underscore the crucial role of fibers in star formation and suggest a hierarchical fragmentation process that extends from the filament to the fibers, and ultimately, to the smallest-scale condensations.

*Keywords:* stars: formation; ISM:filament: fragmentation; fiber: condensations.

## 1. INTRODUCTION

Filamentary structures are prevalent in the molecular clouds of the Milky Way, and recognized to play a vital role in both low-mass and high-mass star formation scenarios (Molinari et al. 2010; André et al. 2010, 2014; Könyves et al. 2020; Liu et al. 2023). *Herschel* dust continuum observations in far/submillimeter bands have demonstrated that prestellar cores and protostars predominantly form in the densest filaments within molecular clouds (e.g., Könyves et al. 2010; Stutz & Gould 2016; Kainulainen et al. 2017; Liu et al. 2018, 2019). Moreover, filaments resolved in nearby star-forming regions exhibit a power-law distribution for both the filament mass function (FMF),  $\frac{dN}{dM} \propto M^{-2.6}$ , and filament line mass function (FLMF),  $\frac{dN}{dm} \propto m^{-2.4}$ , respectively (André et al. 2019). This may naturally result in a power-law distribution of core masses (André et al. 2019; Arzoumanian et al. 2019), i.e., the core mass function (CMF). Accordingly, the CMF has also been observed to agree well with the stellar initial mass function (IMF) in the range of low to intermediate stellar masses ( $\sim 0.1 - 5 M_\odot$ , Könyves et al. 2010), as previously reported (e.g., Motte et al. 1998; Alves et al. 2007; André et al. 2007). Nonetheless, this agreement has been observed to be challenging in regions of massive star formation (e.g., Zhang et al. 2015; Motte et al. 2018; Sanhueza et al. 2019; Pouteau et al. 2022, 2023; Mai et al. 2024; Louvet et al. 2024), with

an evident deviation between the CMF and the IMF in terms of the slope at the high-mass end. In this context, filaments play a critical role in the star formation process, setting up its initial conditions. However, their formation, evolution into substructures, dense cores, and ultimately stars, is still not fully understood.

Substantial progress has been made in deciphering the evolution of filaments. When scrutinized at a high enough resolution, an increasing number of studies reveal a new type of dense molecular filaments at small scales, which are called dense fibers. These fibers are detected across the mass spectrum of clouds, for example, in low-mass clouds (Hacar et al. 2013; Arzoumanian et al. 2013; Fehér et al. 2016), intermediate mass clusters (Fernández-López et al. 2014; Hacar et al. 2017), and high-mass star-forming regions (Hacar et al. 2018; Treviño-Morales et al. 2019; Shimajiri et al. 2019; Li et al. 2022; Cao et al. 2022). As summarized by Hacar et al. (2023), the fibers typically display sub-parsec lengths ( $L \lesssim 1 \text{ pc}$ ), and have line masses near the critical value (Hacar et al. 2018) for hydrostatic equilibrium. Fibers also exhibit high central gas densities  $n_0 > 10^4 \text{ cm}^{-3}$ , and small characteristic widths (full width half maximum (FWHM)  $< 0.1 \text{ pc}$ ; see Hacar et al. 2018, measured in the dense gas tracer,  $\text{N}_2\text{H}^+$  (1-0)). It is interesting to note that the width of filaments or fibers depends on the gas tracer investigated. The widths are observed to be narrower for dense gas tracers, such as

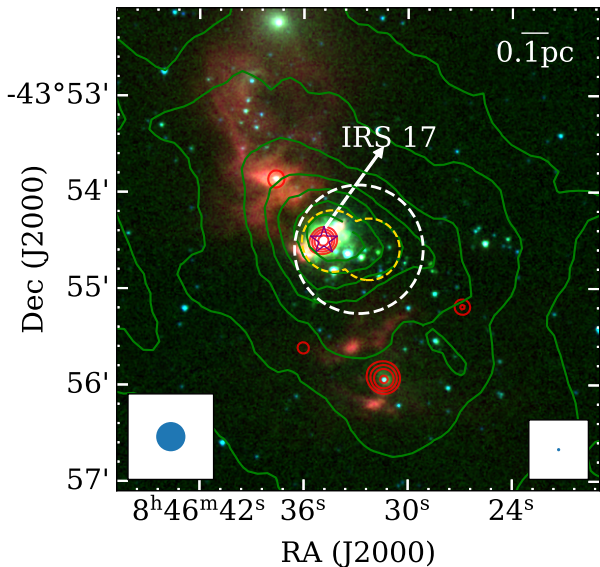


**Figure 1.** *Spitzer* three-colour composite image using  $8\ \mu\text{m}$  (red),  $4.5\ \mu\text{m}$  (green) and  $3.6\ \mu\text{m}$  (blue) of the IRS 17 region. The *Herschel*  $250\ \mu\text{m}$  and  $1.28\ \text{GHz}$  MeerKAT emission (Padmanabh et al. 2023) are shown as the green and red contours, respectively. The white and yellow dashed circle represent the field of views (FoV) of the ATOMS and QUARKS data, respectively (see Fig. 2). The purple star symbol shows the location of IRS 17 source. The resolutions of  $8\ \mu\text{m}$  and  $250\ \mu\text{m}$  are shown at the bottom right and bottom left corners, respectively.

$\text{H}^{13}\text{CO}^+(1-0)$  and  $\text{N}_2\text{H}^+(1-0)$  as compared to the low-density gas tracers like  $^{13}\text{CO}(1-0)$  and  $\text{C}^{18}\text{O}(1-0)$  (Shimajiri et al. 2023).

Fibers correspond to the hierarchical substructure within larger and more massive filaments (e.g. André et al. 2014). Whether fibers or larger filaments form first remains a subject of debate due to the existence of two possibilities. That is, hierarchical fiber structures could arise either from top-down fragmentation due to the self-gravity of their parent filament (Hacar et al. 2013; Tafalla & Hacar 2015), or from a bottom-up process whereby gravitational collapse assembles larger filaments from gas containing pre-existing fibers (Smith et al. 2014).

In addition to dense fibers, dense cores are viewed as crucial substructures of filaments where stars form. The spacing of prestellar cores in star-forming filaments is generally observed to be non-periodic (e.g., André et al. 2014; Könyves et al. 2020), though a few examples of quasi-periodic chains of dense cores have been reported (Tafalla & Hacar 2015; Zhang et al. 2020; Liu et al. 2019; Chung et al. 2023; Yoo et al. 2023). Theoretically, periodic core spacing is predicted by standard semi-analytic cylinder fragmentation models within the framework of

gravitational instability of filaments (e.g., Stodólkiewicz 1963; Jackson et al. 2010; Liu et al. 2018). This discrepancy between observations and simple theoretical predictions may be attributed to the presence of hierarchical fibers within larger filaments (Clarke et al. 2020). Therefore, examining the substructures (i.e., fibers, and cores) of parental filaments is beneficial in understanding the evolution of filaments into cores and ultimately stars.

The target of this work is the IRAS 08448-4343 protocluster (see Fig. 1), which is part of the Vela Molecular Ridge-D (VMR-D) cloud (Murphy & May 1991) located at  $\sim 1.2 \pm 0.1\ \text{kpc}$  (Liu et al. 2024). This distance is consistent with the range of  $0.7$  to  $1.2\ \text{kpc}$  estimated by Liseau et al. (1992) using photometric distance methods. The IRAS 08448-4343 protocluster clump has a molecular gas mass of  $\sim 116\ M_{\odot}$  within a size of  $0.5\ \text{pc}$ , which have been scaled to the distance adopted here (e.g., Faúndez et al. 2004; Liu et al. 2020a). This protocluster corresponds to a bright infrared (IR) source, IRS 17, identified by Liseau et al. (1992) as an intermediate-mass Class I YSO object according to its luminosity of  $\sim 10^3\ L_{\odot}$  (Liseau et al. 1992; Massi et al. 1999). Near-IR observations reveal that more than 20 jet knots are associated with IRS 17 (# 57 in Lorenzetti et al. 2002 and Giannini et al. 2005). The *Spitzer* three-color image in  $3.6/4.5/8.0\ \mu\text{m}$  (see Fig. 1) displays an IR-bright patch and point sources surrounding IRS 17. Furthermore, the IRS 17 region appears as a compact source in radio centimeter emission (e.g., at  $6\ \text{cm}$ , Mottram et al. 2007), which is confirmed by  $1.28\ \text{GHz}$  radio emission (see red contours in Fig. 1), retrieved from the MeerKAT Galactic Plane Survey (Padmanabh et al. 2023; Goedhart et al. 2024). This suggests strong feedback from ionized gas excited by the IRS 17 protocluster. From *Herschel*  $250\ \mu\text{m}$  emission, the molecular cloud hosting the IRS 17 region appears as a clumpy structure elongated along the northeast-southwest direction. This elongation is manifested as a filamentary structure (hereafter the IRS 17 filament) when observed in ALMA 3-mm continuum image at a resolution of  $\sim 2''$  (Liu et al. 2024).

In this work, we investigate the role of small-scale fibers in the evolution of the IRS 17 filament into cores/condensations, leveraging on the combination of the ALMA 3-mm and our new 1.3-mm observations (see below). This paper is structured as follows: observations are described in Section 2; the results and analysis are presented in Section 3; the discussion is followed in Section 4; and finally the summary and conclusion are given in Section 5.

## 2. ALMA OBSERVATIONS

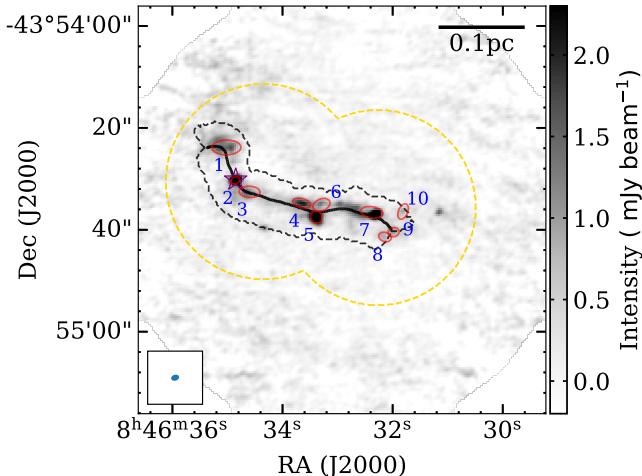


**Figure 2.** 3-mm dust continuum image of the IRS 17 protocluster region from the ATOMS survey. The black solid and dotted lines respectively indicate the footprint and skeleton of the IRS 17 filament obtained with the *getsf* algorithm on the 3-mm dust continuum data. The yellow overlapping circles represent the FoV of the QUARKS survey and the red ellipses represent 10 dense cores within the IRS 17 filament footprint, which were identified by Liu et al. (2021).

The IRS 17 region was observed as part of the ALMA Three-millimeter Observations of Massive Star-forming regions (ATOMS) survey, which targeted 146 active massive protoclusters regions with the ALMA 7-m Atacama Compact Array (ACA) and the 12-m array in the 3-mm band (Liu et al. 2020a). The data were calibrated in CASA 5.6 (McMullin et al. 2007). The ACA and 12-m array data were jointly imaged and cleaned using natural weighting for  $p_{\text{limit}} = 0.2$ , in the CASA *tclean* task, for both continuum images and line cubes. The combined data for the IRS 17 region have a field of view (FoV) and a maximum recoverable scale both of  $\sim 80''$  or 0.5 pc at the distance of IRS 17 (e.g.;  $1.2 \pm 0.1$  kpc). The combined continuum data have a synthesized beam size of  $1.6'' \times 1.2''$ , and a typical sensitivity of  $rms \sim 0.2$  mJy beam $^{-1}$ . The  $\text{H}^{13}\text{CO}^+$  (1–0) line cube, used here for kinematics analysis, has a synthesized beam size of  $1.8'' \times 1.4''$  and a sensitivity of  $rms \sim 8$  mJy beam $^{-1}$  at a velocity resolution of  $\sim 0.2$  km s $^{-1}$ . Details on the observing setups of the survey and its data reduction can be found in Liu et al. (2020a,b, 2021, 2022a,b).

IRS 17 was also observed as part of the Querying Underlying mechanisms of massive star formation with ALMA-Resolved gas Kinematics and Structures (QUARKS) survey, complementing the ATOMS survey with higher angular resolution ( $\sim 0.3''$ ). The observations were carried out with both the ACA and 12-m arrays (Liu et al. 2024). In particular, the elongated spa-

tial extent of the IRS 17 region was covered by two pointings, each of which has a field of view of  $40''$  or 0.2 pc (see the yellow curve in Fig. 2), and a maximum recoverable scale of  $\sim 20''$  or 0.1 pc. The ACA and 12-m data were independently calibrated in CASA 6.5, and then jointly imaged and cleaned using the CASA *tclean* task for both continuum images and line cubes. The combined ACA and 12-m continuum data for the IRS 17 region have a synthesized beam size of  $0.34'' \times 0.33''$ , corresponding to  $\sim 400$  au at a distance of the source. The sensitivity of the continuum data is  $\sim 0.15$  mJy beam $^{-1}$ , which translates to a mass sensitivity of  $\sim 10^{-3} M_{\odot}$  for a dust temperature of  $\sim 25$  K (see Sect. 3.2.1 for the detailed mass calculation). Moreover, the QUARKS survey includes the data of major lines at 1.3 mm, such as  $\text{N}_2\text{D}^+$ , DCN,  $\text{H}_2\text{CO}$ , and  $^{13}\text{CS}$  (see Table 1 of Liu et al. 2024). The native velocity resolution of these line data is 0.6–0.7 km s $^{-1}$ . However, these line data have low detection rates in the IRS 17 region, and hence are considered only for ancillary analysis. Details on the observing setups of the survey and data reduction are described in Liu et al. (2024) and Xu et al. (2024a).

### 3. RESULTS AND ANALYSIS

#### 3.1. IRS 17 filament seen in ATOMS 3-mm continuum

Figure 2 shows the 3-mm continuum map of the IRS 17 protocluster region (also refer to Fig. 7a). The IRS 17 filament extends from the northeast to the southwest. To identify this filament, the *getsf* extraction algorithm (Men’shchikov 2021) was used. This algorithm has been widely employed in previous studies (Xu et al. 2023, 2024a; Dewangan et al. 2024; Louvet et al. 2024) due to its effectiveness in handling uneven noise background, separating blended sources/filaments, and extracting extended emission features. After applying the *getsf* to the 3-mm continuum map, we obtained a single filament skeleton and its footprint, that are shown in Fig. 2 as the black line and the dashed contour, respectively. The filament parameters measured by the *getsf* algorithm are listed in Table 1. These include the center positions, length, width, and integrated flux. The IRS 17 filament has a length of  $\sim 5 \times 10^4$  au (0.26 pc) and a width of  $\sim 4 \times 10^3$  au (0.02 pc). The tabulated widths refer to the mean values of the median widths obtained from both side by the *getsf* algorithm. Note that the median width corresponds to half-power diameters estimated directly from the profiles using *getsf*, without any fitting, such as Gaussian or Plummer fitting (Men’shchikov 2021).

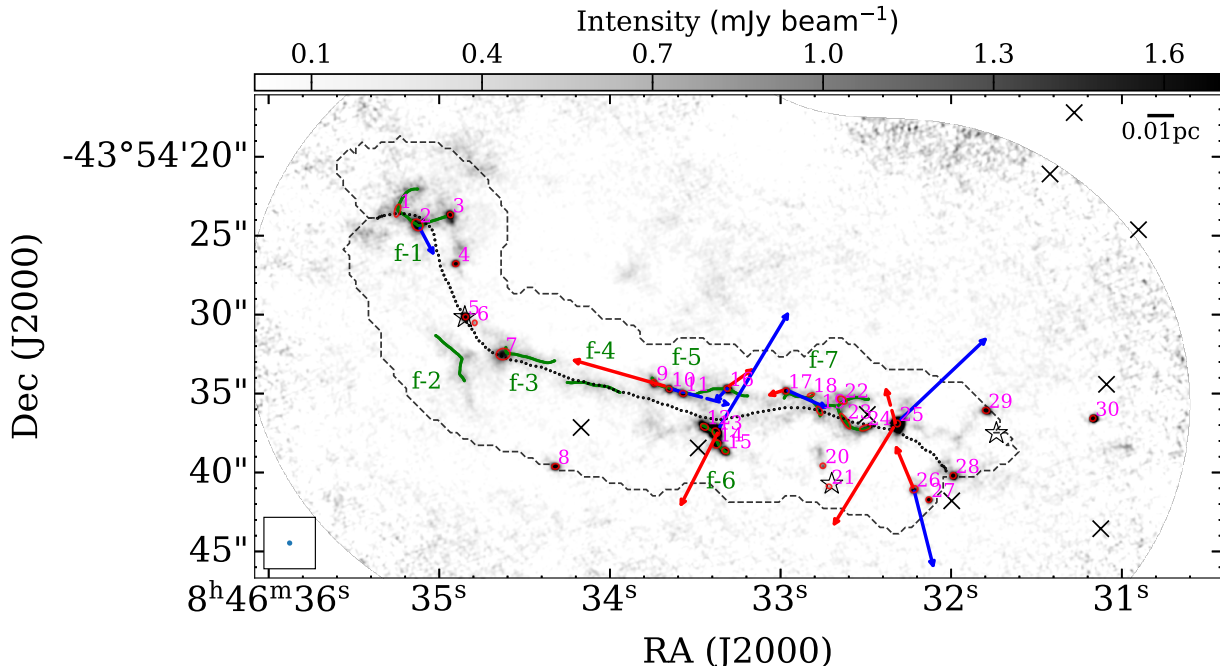


**Figure 3.** 1.3-mm dust continuum image from the QUARKS survey. The black dotted line shows the skeleton of the IRS 17 filament, and green solid lines represent the dense fibers. Red ellipses show the condensations identified by the *getsf* and SExtractor algorithm. The black stars and crosses are the YSO Class I/0 objects and IRAC point-like sources as candidate YSOs (Strafella et al. 2010, 2015), respectively. The solid and dashed arrows represent the outflows identified either from CO (2–1) or SiO (5–4), respectively (see Fig. 9). The synthesized beam size and the scale-bar are shown in left bottom and top right, respectively.

Assuming that 3-mm continuum emission is optically thin and arises primarily from thermal dust radiation, we can compute the mass of the IRS 17 filament using the expression

$$M = \frac{S_{\nu}^{\text{int}} D^2 R_{\text{gd}}}{\kappa_{\nu} B_{\nu}(T_{\text{dust}})}, \quad (1)$$

where the integrated flux,  $S_{\nu}^{\text{int}}$ , is derived from 3-mm continuum emission,  $D$  is the source distance, the ratio of gas-to-dust,  $R_{\text{gd}}$ , is assumed to be 100, and the dust opacity,  $\kappa_{\nu}$ , is taken as  $0.18 \text{ cm}^2 \text{ g}^{-1}$  at 3 mm (Ossenkopf & Henning 1994; Liu et al. 2021).  $B_{\nu}(T_{\text{dust}})$  is the Planck function for a given dust temperature. Here,  $T_{\text{dust}} = 25 \text{ K}$  is adopted for the IRS 17 filament, the same as its natal clump’s average temperature derived from the spectral energy distribution (Faúndez et al. 2004).

The calculated mass of the IRS 17 filament is  $M_{\text{F}} \sim 24.9 M_{\odot}$ . The line mass ( $m_{\text{F}}$ ) was computed as  $m_{\text{F}} = M_{\text{F}}/L_{\text{F}} \sim 95.8 M_{\odot} \text{ pc}^{-1}$ . This line mass is around 2–3 times higher than those inferred from *Herschel* observations toward low mass star forming filaments, such as Musca (see Fig. 4 of Cox et al. 2016), and Taurus B211/3 (see Fig. 2 of Palmeirim et al. 2013) but lower than those toward high-mass counterparts such as Orion ISF (Stutz & Gould 2016). Assuming that the FMF could natu-

rally produce the CMF, which in turn is proportional to the IMF (André et al. 2019), this result suggests that the IRS 17 filament is an intermediate-mass star forming region. Additionally, it is also consistent with the presence of the intermediate-mass IR bright YSO (i.e., the IRS 17 point source). Moreover, assuming a uniform density distribution for the filament, the average number density ( $\langle n_{\text{F}} \rangle$ , see Col.4 in Table 2) relates to  $M_{\text{F}}/(\pi r_{\text{F}}^2 L)$ , where  $r_{\text{F}}$  represents the radius of the filament ( $r_{\text{F}} = \frac{1}{2} W_{\text{F}}$ ).

Within the footprint of the IRS 17 filament, ten 3 mm dense cores are identified (see Fig. 2). These cores were identified by Liu et al. (2021), who utilized both the *astrodendro* algorithm and the *CASA imfit* function together for the identification. These cores have a mass range of  $0.3\text{--}2.5 M_{\odot}$  (see Table 4 of Liu et al. 2021) with sizes of the order of 0.01 pc. However, one of the cores (i.e., #2, see Fig. 2), with a mass of  $2.0 M_{\odot}$ , is associated with the ionized gas excited by the intermediate-mass IRS 17 protocluster. Therefore, its mass could be overestimated by assuming that 3-mm continuum emission arises primarily from dust thermal emission. As such, the mass of this core should be interpreted with caution. It is worth noting that the same issue could influence the mass calculation of the natal filament, but

**Table 1.** Parameters of filament and fibers obtained with the *getsf* algorithm

Name	Position <sup>a</sup>		$L^b$		$W^b$		Aspect ratio	$S_{\nu}^{\text{int}}$ (mJy)	Data Source
	$\alpha$ (J2000)	$\delta$ (J2000)	( $''$ )	( $\times 10^3$ au)	( $''$ )	( $\times 10^3$ au)			
Filament	08:46:33.84	-43:54:32.53	$43.5 \pm 4.4$	$53.6 \pm 5.4$	$3.2 \pm 1.5$	$3.9 \pm 1.9$	13.6	$43.8 \pm 4.4$	3 mm
fiber									1.3 mm
1	08:46:35.12	-43:54:23.44	$5.5 \pm 0.6$	$6.7 \pm 0.7$	$1.5 \pm 0.6$	$1.9 \pm 0.8$	3.7	$103.8 \pm 10.4$	
2	08:46:34.92	-43:54:32.46	$3.8 \pm 0.4$	$4.6 \pm 0.5$	$1.2 \pm 0.3$	$1.5 \pm 0.4$	3.1	$34.8 \pm 3.5$	
3	08:46:34.47	-43:54:33.00	$3.5 \pm 0.4$	$4.3 \pm 0.4$	$1.2 \pm 0.5$	$1.5 \pm 0.6$	3.0	$44.5 \pm 4.5$	
4	08:46:34.05	-43:54:34.54	$3.5 \pm 0.4$	$4.3 \pm 0.4$	$1.1 \pm 0.3$	$1.3 \pm 0.4$	3.5	$27.2 \pm 2.7$	
5	08:46:33.49	-43:54:34.66	$6.6 \pm 0.7$	$8.0 \pm 0.8$	$0.9 \pm 0.6$	$1.1 \pm 0.8$	7.8	$78.9 \pm 7.9$	
6	08:46:33.40	-43:54:38.20	$2.6 \pm 4.4$	$3.2 \pm 0.3$	$0.8 \pm 0.2$	$1.0 \pm 0.3$	3.2	$50.5 \pm 5.1$	
7	08:46:32.69	-43:54:36.17	$7.1 \pm 0.7$	$8.7 \pm 0.9$	$1.3 \pm 0.8$	$1.5 \pm 0.9$	5.8	$111.5 \pm 11.2$	

<sup>a</sup> The central coordinate of IRS 17 filament and fibers.

<sup>b</sup> The lengths and widths are derived from the footprints of filament and the fibers extracted with the *getsf* algorithm.

**Table 2.** Estimated properties and velocity information of filament and fibers

Name	$M$	$m$	$m_{\text{crit}}^{\text{tur}}$	$\langle n \rangle$	$v_{\text{lsr}}^*$	$\sigma_{\text{obs}}^*$
	( $M_{\odot}$ )	( $M_{\odot} \text{ pc}^{-1}$ )	( $M_{\odot} \text{ pc}^{-1}$ )	( $\times 10^7 \text{ cm}^{-3}$ )	( $\text{km s}^{-1}$ )	( $\text{km s}^{-1}$ )
Filament	$24.9 \pm 5.0$	$95.8 \pm 19.2$	$70.7 \pm 29.1$	$0.49 \pm 0.15$	$3.26 \pm 1.15$	$0.39 \pm 0.25$
fiber						
1	$2.54 \pm 0.51$	$77.0 \pm 15.4$	$178.7 \pm 47.6$	$1.70 \pm 0.34$	$5.11 \pm 0.30$	$0.62 \pm 0.32$
2	$0.83 \pm 0.17$	$37.7 \pm 7.5$	$67.1 \pm 5.6$	$1.29 \pm 0.10$	$5.31 \pm 0.20$	$0.38 \pm 0.11$
3	$1.09 \pm 0.22$	$51.9 \pm 10.4$	$50.6 \pm 29.1$	$1.82 \pm 0.36$	$3.25 \pm 0.87$	$0.33 \pm 0.25$
4	$0.66 \pm 0.13$	$31.4 \pm 6.3$	$47.6 \pm 22.5$	$1.47 \pm 0.15$	$3.11 \pm 0.79$	$0.32 \pm 0.22$
5	$1.92 \pm 0.38$	$49.2 \pm 9.8$	$70.7 \pm 24.6$	$3.20 \pm 1.60$	$3.39 \pm 0.27$	$0.39 \pm 0.23$
6	$1.23 \pm 0.25$	$82.0 \pm 16.4$	$90.0 \pm 7.9$	$6.21 \pm 0.62$	$3.10 \pm 0.40$	$0.44 \pm 0.13$
7	$2.72 \pm 0.54$	$61.8 \pm 12.4$	$94.2 \pm 9.1$	$2.24 \pm 0.89$	$2.33 \pm 0.64$	$0.45 \pm 0.14$

\* The velocity centroid and velocity dispersion measured from the  $\text{H}^{13}\text{CO}^+$  line emission of the ATOMS survey.

not significantly. This is because the absolute value of the mass of the related core, which encompasses most of the ionized gas, is much lower than the filament mass. Furthermore, these dense cores within the filament do not exhibit a periodic chain-like distribution as seen in Fig. 2, which will be discussed in Sect. 4.1.

### 3.2. *Fibers and condensations in QUARKS 1.3-mm dust continuum*

Figure 3 displays the QUARKS 1.3-mm dust continuum map of the IRS 17 protocluster region (also refer to Fig. 7b). The IRS 17 filament can still be observed in 1.3-mm emission, confirming the filamentary nature seen in 3-mm emission. This filament presents several

substructures in 1.3-mm observations, including small-scale fibers and dense condensations. To identify them, the *getsf* algorithm was applied to the 1.3-mm dust continuum map. The bona fide fibers were identified based on the following three criteria: i) the peak flux of a fiber is detected at least at 3 *rms* significance level, ii) the length of a fiber is at least 3 times the synthesized beam size at 1.3-mm, and iii) the aspect ratio is at least 3.

As a result, a total of 7 fibers and 24 condensations were obtained (Fig. 3). However, upon a careful visual inspection, several dense fibers and condensations appear not be recognized by the *getsf* algorithm. Specifically, a network of fibers between condensations 25, 28 and 29 is seen in the figure but not detected by *getsf* (see

Fig. 8). This is because they are disjoint due to low peak emission of  $< 3\text{ rms}$  along each individual fiber in the network. In addition, this network of fibers does not appear as velocity coherent structures, which can be found in the  $\text{H}^{13}\text{CO}^+$  (1–0) velocity field map (see Fig. 4b). To recover the missing condensations, another source extraction method, SExtractor (Bertin & Arnouts 1996; Barbary 2016) was utilized, as adopted in other studies (e.g.; Contreras et al. 2013; Urquhart et al. 2014; Xu et al. 2024a). This approach identified 6 additional condensations (i.e., C1, C18, C19, C22, C23, and C24), leading to a total of 30 condensations (refer to Table 4). Except for C30, all condensations are located in the IRS 17 filament (see Fig. 3). The parameters measured by the *getsf* for fibers are listed in Table 1, including the center positions, length, width, and integrated flux. The parameters by the *getsf* or the SExtractor for condensations are given in Table 4, including the center positions, size, integrated flux and peak flux.

The gas kinematics of the IRS 17 filament and the identified fibers was inferred using the  $\text{H}^{13}\text{CO}^+$  (1–0) molecular line transition from the ATOMS survey. The velocity centroid and the velocity dispersion of both filament and the fibers are tabulated in Table 2.

### 3.2.1. Derived parameters of fibers and condensations

Following Eq. 1, we quantified the mass of fibers ( $M_f$ ) and condensations ( $M_c$ ) from the integrated flux at 1.3-mm, given the corresponding dust opacity  $\kappa_{1.3\text{mm}} = 0.899\text{ cm}^2\text{ g}^{-1}$  (Ossenkopf & Henning 1994) and the temperature of 25 K. Using the same approach as for the IRS 17 filament, we can estimate for fibers the line mass ( $m_f$ ), and the average number density ( $\langle n_f \rangle$ ). For condensations, assuming a uniform spherical density distribution, their number density can be inferred as  $n_c = \frac{3M_c}{4\pi R_c^3 \mu m_H}$ , the mean molecular weight  $\mu = 2.8$ , and  $m_H$  is the mass of the hydrogen atom.  $R_c$  is the radius of each condensation, given by  $R_c = \sqrt{R_{eff}^2 - (1/4 \ln 2) b_{maj} \times b_{min}}$  (Lu et al. 2014), where the effective radius,  $R_{eff} = \sqrt{FWHM_{maj} \times FWHM_{min}/2}$ .

Table 2 and Table 4 outline the parameters derived above for the fibers and condensations, respectively. The fibers exhibit a length range of  $\sim 3000$  to  $9000$  au, with a median value of  $\sim 4500$  au. Their width varies from about  $\sim 1000$  to  $2000$  au, with a median of roughly  $1400$  au. The mass of these fibers spans from  $0.66$  to  $2.72 M_\odot$ , with a median of  $\sim 1.2 M_\odot$ . The line mass ( $m_f$ ) extends from  $31.4$  to  $82.0 M_\odot\text{ pc}^{-1}$ , with a median of  $51.9 M_\odot\text{ pc}^{-1}$ . The average number density of fibers varies within a range of  $1.3 \times 10^7 - 6.2 \times 10^7\text{ cm}^{-3}$  with a median of  $1.8 \times 10^7\text{ cm}^{-3}$ . As for the condensations,

their effective radius and number density have a range of  $[180, 410]$  au, and  $[7.3 \times 10^7, 2.7 \times 10^9]\text{ cm}^{-3}$ , respectively. The mass of these condensations spans from  $0.02$  to  $1.31 M_\odot$ , with a median of  $0.11 M_\odot$ . These results for condensations are comparable to values derived in other intermediate-mass star-forming regions, such as the condensation mass ranges from  $0.1$  to  $0.4 M_\odot$  in the TUKH122 prestellar core in the Orion A cloud (Ohashi et al. 2018), and the mass ranges from  $0.01$  to  $0.2 M_\odot$  in the NGC 2071 IR (Cheng et al. 2022). It is worth noting here that the derived masses could be underestimated for two likely reasons (1) the assumed average clump temperature of 25 K could be on the higher side for some of the non-YSO bearing condensations and (2) the high-resolution interferometric observations could have filtered out diffuse, low-density emission. Additionally, we cannot rule out over estimation of mass for condensations harboring protostars where temperatures could be as high as 50 K.

### 3.2.2. Classification of fertile fibers

As depicted in Fig. 3, some fibers accommodate dense condensations, which are likely precursors to star formation. Given their spatial association with condensations, fibers can be classified as “fertile” or “sterile” (Hacar et al. 2013; Tafalla & Hacar 2015). According to these authors, fertile fibers generally have a higher line mass and contain at least three dense condensations, unlike their sterile counterparts. In the IRS 17 filament, four fibers (namely, f1 and f5–7) are classified as fertile, while the rest are considered sterile.

We applied the minimum-spanning tree (MST) method (Barrow et al. 1985; Wang et al. 2016; Sanhueza et al. 2019; Liu et al. 2022a; Xu et al. 2024b) to estimate the separation between condensations within the fertile fibers. The MST approach (e.g. Dib & Henning 2019) determines the shortest distances that can possibly connect each of the objects in a given field. The estimated separations of condensations in the four fertile fibers range from approximately  $850$  to  $3450$  au, with a median of around  $1600 \pm 600$  au, where the error is the standard deviation of their separations.

### 3.3. Filament and fibers seen in molecular gas emission

Figure 4 presents the moment maps of  $\text{H}^{13}\text{CO}^+$  (1–0) toward the IRS 17 filament observed in 3-mm dust continuum. The  $\text{H}^{13}\text{CO}^+$  (1–0) line, with a critical density of  $\sim 10^5\text{ cm}^{-3}$  (Sanhueza et al. 2012), allows us to trace relatively dense gas compared to CO and its isotopologue lines (Shimajiri et al. 2023). The Moment 0 map of  $\text{H}^{13}\text{CO}^+$  (1–0) reveals that relatively dense gas emission spans the entire filament, except for the region

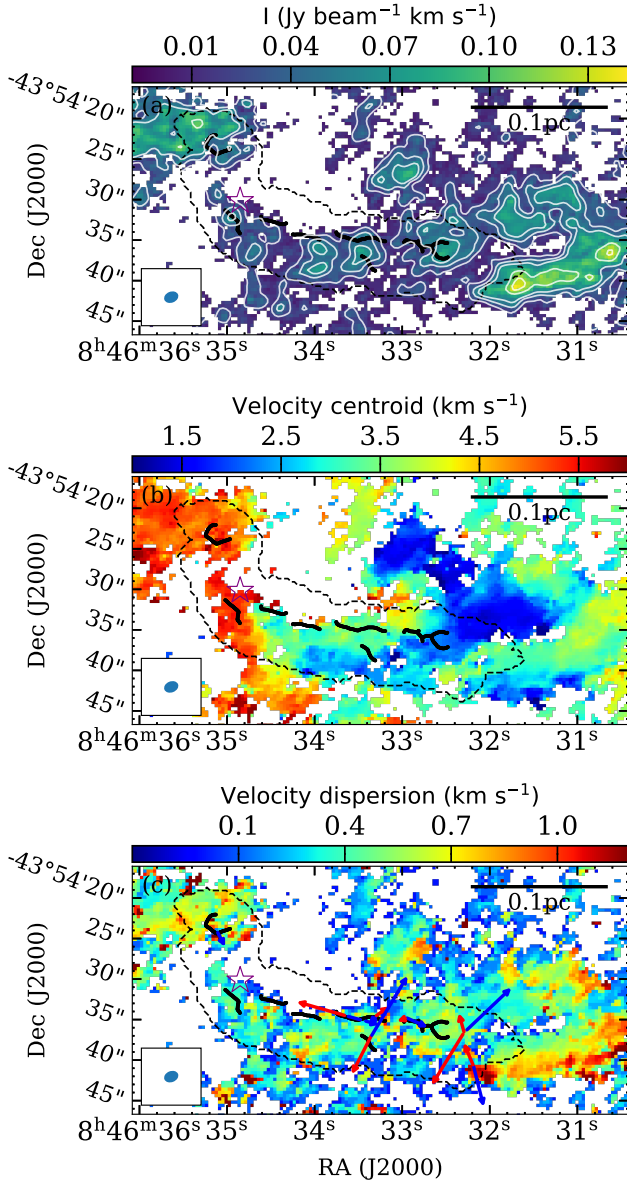


**Figure 4.** Moment maps of  $\text{H}^{13}\text{CO}^+$  from the ATOMS survey. The velocity range of  $\text{H}^{13}\text{CO}^+$  emission is set to  $[1, 6] \text{ km s}^{-1}$ , which correspond to the velocity channels with a signal-to-noise ratio above  $3 \text{ rms}$  in the average spectrum over the entire region. The  $\text{rms}$  defined as the standard deviation within 50 channels free of line emission ( $\sim 0.01 \text{ Jy beam}^{-1}$ ). The black dashed and solid lines represent the IRS 17 filament footprint and fibers, respectively. The ATOMS beam and  $0.1 \text{ pc}$  scale-bar are shown in left bottom and top right, respectively. (a) Integrated intensity (Moment 0) map. The white contour levels start at  $3 \text{ rms}$  ( $\sim 0.01 \text{ Jy beam km s}^{-1}$ ), and following as  $[6, 9, 12, 15] \text{ rms}$ . (b) Velocity centroid (Moment 1) map. (c) Velocity dispersion (Moment 2) map. The solid and dashed arrows represent the outflows identified either from  $\text{CO} (2-1)$  or  $\text{SiO} (5-4)$ , respectively (see Fig. 9)

around the intermediate-mass protocluster (see the purple star symbol in Fig. 4) where protostellar feedback is supposed to be strong. In addition, near the protocluster,  $\text{H}^{13}\text{CO}^+ (1-0)$  emission does not cover the full filament footprint.

This could be attributed to the missing flux in the interferometric data or to the clean-up by the outflows with a wide opening angle from the IRS 17 protocluster (see the red-shifted high-velocity CO gas component related to the protocluster in Fig. 9a). As a consequence, though the  $\text{H}^{13}\text{CO}^+$  emission appears to be primarily distributed south of the crest of the IRS 17 filament, particularly in the southwest region, the morphology and the location of identified fibers indicate that it traces the 3-mm filament.

In the velocity field (Moment 1) map of  $\text{H}^{13}\text{CO}^+$ , the molecular gas shows a coherent velocity distribution along the dust emission filament. Similar to the velocity structure of the filamentary cloud in Taurus, presented in Hacar et al. (2013), multiple velocity components are seen in the IRS 17 filament, ranging from  $1.5$  to  $5.5 \text{ km s}^{-1}$  (see  $\text{H}^{13}\text{CO}^+$  velocity field in Fig 4b), suggesting complex gas structures. Here, these velocity components can also be observed in the velocity map of the DCN line (see Fig. 10) from the QUARKS survey at higher angular resolution but lower detection rate than the same map of the  $\text{H}^{13}\text{CO}^+$  line from the ATOMS survey. Additionally, a distinct velocity gradient is also observed along the filament, with increasing velocity centroid from west to east. Despite this complex gas kinematics observed in the filament, the individual identified fibers are seen to be velocity coherent sub-structures (the velocity centroid ranges from  $2.3$  to  $5.3 \text{ km s}^{-1}$ , see Col. 5 in Table 2). Furthermore, the detected fibers are seen to be in three bundles with similar kinematics, (1) f1–2 corresponding to a velocity of  $\sim 5.0 \text{ km s}^{-1}$ , (2) f3–6 with velocity  $\sim 3.1 \text{ km s}^{-1}$ , and (3) f7 with velocity  $\sim 2.3 \text{ km s}^{-1}$ .

In Fig. 4c, we present the velocity dispersion (Moment 2) map of  $\text{H}^{13}\text{CO}^+ (1-0)$ . Within the IRS 17 dust filament, molecular gas has a median velocity dispersion of  $0.39 \pm 0.25 \text{ km s}^{-1}$ , indicating transonic gas motions compared to the typical thermal sound speed of  $0.3 \text{ km s}^{-1}$  at a temperature of  $25 \text{ K}$ . The locally enhanced gas motions likely result from local active star formation feedback, including strong ionized gas from the intermediate-mass IRS 17 protocluster (see the purple star symbol in Fig. 4c) and outflows (see the arrows in Fig. 4c) distributed along the filament. Specifically, the northeastern region near the protocluster bears more pronounced supersonic motions due to ionized gas feedback, while several outflows scattered along the filament

make local gas motions enhanced. Additionally, several regions outside the filament appear even higher supersonic velocities (i.e.,  $\sim 1 \text{ km s}^{-1}$ ), which deserves further investigation in the future. [Hacar et al. \(2018\)](#) investigated the massive Integral Shape Filament (ISF) in Orion, which experiences more intense star formation feedback. Their observations of the ISF fibers using the  $\text{N}_2\text{H}^+$  (1-0) transition revealed transonic non-thermal velocity dispersions ( $0.24 \text{ km s}^{-1}$  on average) relative to the local temperature. Given this, the velocity dispersion estimated from  $\text{H}^{13}\text{CO}^+$  (1-0) appears reasonable for the IRS 17 region.

### 3.4. Stability of the IRS 17 filament and fibers

The gravitational stability of filaments and fibers can be quantitatively evaluated under an ideal model of isothermal and infinite cylinders using the parameter of the critical line mass ( $m_{\text{crit}}$ , [Stodólkiewicz 1963](#); [Ostriker 1964](#)). Filaments and fibers with an observed line mass greater than  $m_{\text{crit}}$  (supercritical) are expected to collapse under their own gravity, while those with an observed line mass less than  $m_{\text{crit}}$  (subcritical) can maintain a hydrostatic equilibrium or become dispersed.

The  $m_{\text{crit}}$  parameter can be expressed as follows ([Stodólkiewicz 1963](#); [Ostriker 1964](#)):

$$m_{\text{crit}} = \frac{2\sigma_{\text{eff}}^2}{G}, \quad (2)$$

where  $G$  represents the gravitational constant and  $\sigma_{\text{eff}}$  is the effective speed of sound to be considered in varied situations. If we consider only the contribution from thermal motions, the term  $\sigma_{\text{eff}}$  can be replaced with the thermal sound speed of gas,  $c_s$ , resulting in the thermal critical line mass:

$$m_{\text{crit}}^{\text{th}} = \frac{2c_s^2}{G} \sim 16.6 \left( \frac{T}{10 \text{ K}} \right) M_{\odot} \text{ pc}^{-1}, \quad (3)$$

where  $T$  is the kinetic temperature of the gas. Here, we assume it to be the same as the average dust temperature of  $T = 25 \text{ K}$ . This yields  $m_{\text{crit}} \sim 41.5 M_{\odot} \text{ pc}^{-1}$ . Compared with the observed line mass, the IRS 17 filament and all the fibers except f2 and f4 are thermally supercritical (see Table 2). It is important to note that the assumed average dust temperature of 25 K is relatively high compared to the estimated temperatures of other intermediate-mass protoclusters, such as NGC 1333 ( $\sim 10 \text{ K}$ ; see Table 2 of [Hacar et al. 2018](#)). However, adopting a temperature of 10 K would render fibers f2 and f4 supercritical, which contradicts their observed nature since no associated condensations are present (see Fig. 2). Therefore, accurate temperature measurements will be essential in future studies to resolve this discrepancy.

If we account for the contribution from non-thermal motions to the stability of the IRS 17 fibers, the term  $\sigma_{\text{eff}}$  can be substituted with the total velocity dispersion,  $\sigma_{\text{tot}}$ , and thus the turbulent critical line mass becomes

$$m_{\text{crit}}^{\text{tur}} = \frac{2\sigma_{\text{tot}}^2}{G} \sim 465 \left( \frac{\sigma_{\text{tot}}}{1 \text{ km s}^{-1}} \right)^2 M_{\odot} \text{ pc}^{-1}. \quad (4)$$

From the  $\text{H}^{13}\text{CO}^+$  (1-0) line data, we obtained an median velocity dispersion of  $\sim 0.39 \pm 0.25 \text{ km s}^{-1}$  within the IRS 17 filament (see Table 2). Using this, we estimate a turbulent  $m_{\text{crit}}^{\text{tur}}$  of  $70.7 \pm 29.1 M_{\odot} \text{ pc}^{-1}$ . Given the complex velocity field and within the quoted uncertainties, the IRS 17 filament could be supercritical, consistent with the fragmentation to fibers hypothesis discussed in Section 4.1. However, the estimated turbulent  $m_{\text{crit}}^{\text{tur}}$  is significantly greater than the observed line mass of fibers within IRS 17 region (except for f3, see Col.3 in Table 2), with a factor of 1.1 to 2.3. This contradicts the observed scenario of gravitational collapse of the fibers and the formation of the detected condensations within them. The discrepancy is likely produced by the ongoing active star formation within IRS 17 filament, where outflows and feedback from ionized gas results in large velocity dispersion. Such high turbulence may not be prevalent during the initial stages of collapse of the small-scale fibers, but is typically close to the sound speed ([Hacar et al. 2013, 2018](#)). The above discussion finds support in the observed cascade of turbulence with the decreasing scale of the density structures ([Larson 1981](#); [Hacar et al. 2023](#); [Luo et al. 2024](#)). The  $\sigma_{\text{tot}}$  follows  $\sigma - L$  ( $\sigma_{\text{tot}} = c_s(1 + \frac{L}{0.5 \text{ pc}})^{0.5}$ ), an empirical relation observed by [Hacar et al. \(2023\)](#) for filaments and fibers, which is akin to the first of Larson's relation for general clouds ([Larson 1981](#)). For the estimated length scale of the IRS 17 fibers, which are significantly less than  $0.05 \text{ pc}$  ( $\sim 10000 \text{ au}$ ),  $\sigma_{\text{tot}} \sim c_s$  making  $m_{\text{crit}}^{\text{tur}} \sim m_{\text{crit}}^{\text{th}}$ . Thus, for the length scale of the IRS 17 fibers, the role of turbulence would be negligible. Summarizing the stability analysis, except f2 and f4, the other IRS 17 fibers are observed to be supercritical consistent with the presence of dense condensations within them. However, we should note that the  $\sigma - L$  has uncertainties of  $\pm 0.2 \text{ pc}$  and  $\pm 0.2$  for the length ( $L$ ) and exponent, respectively ([Hacar et al. 2023](#)).

Note that magnetic fields could potentially have a considerable impact on the stability of the fibers. However, our analysis above ignores the magnetic fields, as such information is not available.

### 3.5. Stability of condensations

The stability of condensations can be evaluated by the virial parameter ( $\alpha_{\text{vir}}$ ) as below ([Bertoldi & McKee](#)

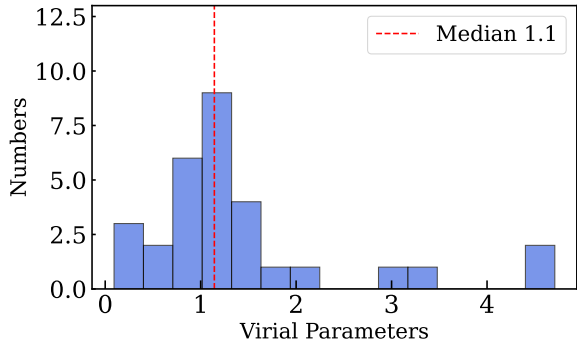


**Figure 5.** Virial parameter distribution of IRS 17 condensations. Only the thermal motion is considered for virial analysis. The red dashed lines represent the median value of virial parameter.

1992):

$$\alpha_{\text{vir}} = \frac{5\sigma_{\text{eff}}^2 R_c}{GM_c}, \quad (5)$$

where  $R_c$  is the condensation radius. The subvirial cores with  $\alpha_{\text{vir}} \leq 2$  will collapse to form stars (Liu et al. 2022a). For the stability analysis of the condensations, one needs to include the contribution from turbulence in the  $\sigma_{\text{eff}}$  term. However, we lack molecular line data (e.g.,  $\text{N}_2\text{H}^+$  (1–0)) at matching angular resolution. Moreover, if IRS 17 fibers exhibit transonic turbulent motions similar to the OrionA ISF fibers as reported by Hacar et al. (2018) using  $\text{N}_2\text{H}^+$  observations, the impact of turbulence on the stability of smaller-scale condensations will become negligible. This is consistent with  $\sigma - L$  scaling (see Section 3.4), where the effect of turbulence would be negligible for the length scales of these sub-structures. Hence, we consider only the thermal motion and replace  $\sigma_{\text{eff}}$  by the sound speed of gas,  $c_s$ . Assuming the same  $c_s$  value (i.e.,  $0.3 \text{ km s}^{-1}$ ) for all condensations in the IRS 17 filament at a temperature of 25 K, we find most (25 of 30, 83 %) of them with  $\alpha_{\text{vir}} \leq 2$ , with a median value of 1.1 (see Fig. 5). This implies that most of identified condensations within the IRS 17 region are gravitationally bound and will undergo collapse unless supported by magnetic field. Moreover, two of the condensations (C5 and C21) are associated with the Class I/0 YSOs (see Fig. 3), and additional seven (i.e., C2, C10, C13, C16, C17, C25 and C26) are associated with outflows identified from the SiO and CO line transitions (see Fig. 9). The association of these YSOs and outflows lends strong support to our understanding that these condensations are potential seeds of star formation. It is worth noting that, as mentioned in Section 3.2.1, the condensations without YSO associated could have lower temperatures possibly down to 10K, while those with YSO as-

sociated could have higher temperature possible up to 50 K. The former case will make the virial parameters about 6 times lower than the current values, and thus does not change the subvirial state of those condensations without YSOs; the latter case will make the virial parameters about 4 times higher, and accordingly make the dynamical state of those condensations with YSOs change to be supervirial.

A point that solicits further discussion is the low masses of the identified condensations (see Table 4). Notwithstanding the issue of assuming a higher dust temperature or factoring in the missing flux of the interferometric observations, for the non-YSO bearing and non-outflow hosting condensations, the estimated masses are similar to those derived for the protostars in NGC 2071 IR by Cheng et al. (2022) using 1.3 mm ALMA observations. As pointed out by these authors, these could be treated as lower limits, since the emission from the protostars could be partially optically thick at 1.3 mm. Furthermore, with the sensitivity and the resolution of the observed data, these detected supercritical ( $\alpha_{\text{vir}} \leq 2$ ) condensations could be just the central cores of Bonnor–Ebert spheres that have steep density profiles (Ohashi et al. 2018). However, one cannot rule out the formation of very low-mass objects from these condensations. The condensations associated with YSOs and outflows, on the other hand, might be undergoing a dynamical process of star formation, as described in various dynamical models of star formation (e.g., Vázquez-Semadeni et al. 2019; Padoan et al. 2020). For instance, the inertial inflow model proposed by Padoan et al. (2020) outlines star formation as a three-step dynamical process: (1) the formation of a gravitationally unstable core, (2) the collapse of this core into a low to intermediate-mass star, and (3) the subsequent accretion of the remaining mass from the natal core onto the star. An exception is the condensation C21, where the estimated mass is too low ( $0.02 \pm 0.01 M_{\odot}$ ) to explain the signature of star formation therein. Given the weak 1.3 mm emission observed, it is highly likely that we are detecting only the peak emission from the central region.

### 3.6. Fragmentation of fibers

Theoretically, semi-analytic linear cylinder fragmentation models, such as the “sausage” instability model (Nagasawa 1987; Jackson et al. 2010), are commonly used to investigate the fragmentation of filamentary structures. The premise of these theoretical models is that the fragmentation of a self-gravitating fluid cylinder can lead to chains of dense cores with nearly periodic

**Table 3.** Derived parameters of fibers

Fiber	Position		$\langle n_0 \rangle^a$ ( $\times 10^8 \text{ cm}^{-3}$ )	$\langle \lambda_{\text{pro}} \rangle^b$ ( $\times 10^3 \text{ au}$ )	H ( $\times 10^2 \text{ au}$ )	$\lambda_{\text{max}}$ ( $\times 10^3 \text{ au}$ )
	$\alpha(\text{J2000})$	$\delta(\text{J2000})$				
f1	08:46:35.12	-43:54:23.44	$2.18 \pm 0.34$	$2.3 \pm 0.4$	$0.7 \pm 0.1$	$1.8 \pm 0.1$
f5	08:46:33.49	-43:54:34.66	$3.18 \pm 0.63$	$1.9 \pm 1.0$	$0.6 \pm 0.1$	$1.2 \pm 0.2$
f6	08:46:33.40	-43:54:38.20	$8.97 \pm 1.42$	$0.9 \pm 0.2$	$0.3 \pm 0.1$	$0.7 \pm 0.1$
f7	08:46:32.69	-43:54:36.17	$2.21 \pm 0.34$	$1.7 \pm 0.2$	$0.7 \pm 0.1$	$1.5 \pm 0.3$

<sup>a</sup> The central density is estimated from the average volume density of condensations within each fiber.

<sup>b</sup> The mean separation between condensations of each fiber, and the errors from the standard deviation of the separations..

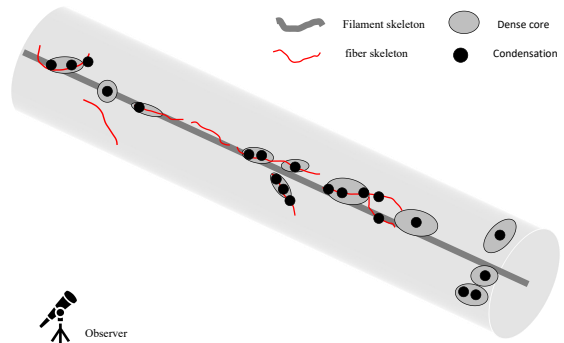
separations (e.g., Chandrasekhar & Fermi 1953; Nagasawa 1987; Jackson et al. 2010). This separation corresponds to the characteristic wavelength ( $\lambda_{\text{crit}}$ ) where the instability grows most rapidly. For an incompressible fluid, perturbation analysis indicates that the critical wavelength emerges at  $\lambda_{\text{crit}} = 11R_{\text{cyl}}$ , where  $R_{\text{cyl}}$  is the cylinder’s radius (e.g., Chandrasekhar & Fermi 1953). In the context of an infinite isothermal gas cylinder, the characteristic wavelength becomes  $\lambda_{\text{crit}} = 22H$ , where  $H = c_s(4\pi G\rho_c)^{-1/2}$  represents the isothermal scale height and  $\rho_c$  is the central mass density along the cylinder’s axis (e.g., Nagasawa 1987; Inutsuka & Miyama 1992; Jackson et al. 2010). For a finite isothermal gas cylinder surrounded by a uniform medium, the value of  $\lambda_{\text{crit}}$  is influenced by the  $R_{\text{cyl}}/H$  ratio. If  $R_{\text{cyl}}/H \gg 1$ , the characteristic separation approximates  $\lambda_{\text{crit}} = 22H$ , aligning with the infinite isothermal gas cylinder model. However, if  $R_{\text{cyl}}/H \ll 1$ , it shifts to  $\lambda_{\text{crit}} = 11R_{\text{cyl}}$ , which corresponds to the incompressible case (e.g., Jackson et al. 2010).

For the IRS 17 filament, we observe no chain of dense cores with a characteristic periodic separation. This suggests that the IRS 17 filament fragmentation into dense cores does not conform to predictions of a simple linear cylinder model. In comparison, predictions of the model as patterns of periodically-spaced dense condensations are evident in the fertile fibers (i.e., f1, and f5–7) within the filament. Hence, assuming the fibers as isothermal and hydrostatic gas cylinders, we take the average volume density of condensations (refer to Col.4 in Table. 3) within each fiber as its central density ( $\rho_c$ ). This allows us to estimate the isothermal scale height for the fibers, yielding  $H \sim 60 \text{ au}$  at a temperature of 25 K. The median radius of the fertile fibers is  $\sim 700 \text{ au}$  ( $1/2 \times W_f$ ), which corresponds to the case of  $R \gg H$ . Hence, the separation of dense condensations within fibers can be predicted from  $\lambda_{\text{max}} = 22H$ . Consequently,

the predicted  $\lambda_{\text{max}}$  for the four fertile fibers ranges from 700 – 1800 au (see Col.7 in table 3). This agrees with the observed typical separation between dense condensations within fertile fibers of  $\sim 900 - 2300 \text{ au}$  (see Col.5 in table 3).

## 4. DISCUSSION

### 4.1. Role of fibers in star formation

**Figure 6.** Cartoon of a cylinder filament model.

Since their discovery (Hacar et al. 2013), subparsec-scale fibers have been reported across varied star-forming regions, including low-mass clouds (Arzoumanian et al. 2013; Fehér et al. 2016), intermediate-mass clusters (Fernández-López et al. 2014; Hacar et al. 2017), and high-mass star-forming regions (Hacar et al. 2018; Treviño-Morales et al. 2019; Li et al. 2022). In good agreement with observations, hydrodynamical simulations of turbulent clouds reveal the natural occurrence of network of fibers within filaments (Smith et al. 2014, 2016). Furthermore, in most regions, the population of observed cores are seen to be predominantly harboured in these fibers, thus highlighting the key role played by these dominant sub-structures in star formation across the mass spectrum. Such a scenario is discerned in

the IRS17 filament, with the observed association between fibers and dense condensations (potential seeds of star formation). A systematic analysis of the internal fibers of the massive Orion-ISF filament and lower-mass objects (e.g., Musca, Taurus) led [Hacar et al. \(2018\)](#) to propose a unified star formation paradigm. In this framework, the observed differences between low- and high-mass clouds naturally emerge from the initial concentration of fibers.

Fibers are proposed to play a critical role in star formation. [Hacar et al. \(2013\)](#) and [Tafalla & Hacar \(2015\)](#) based on their observations of L1495/B213 filamentary complex in Taurus, infer a hierarchical fragmentation process termed ‘fray and fragment’, where the filamentary clouds first fragment to fibers (sub-filaments) which further fragment to dense cores. The above scenario of the impact of fibers on the fragmentation of filaments finds strong support in the numerical study discussed in [Clarke et al. \(2020\)](#).

As shown by these authors, in contrast to the classical filament fragmentation models, the presence of fibers as the intermediate fragmentation stage results in the absence of a strong imprint of quasi-periodic cores in filaments.

The above picture is aptly captured in the cartoon presented in [Fig. 6](#), which explains the observed features in the IRS17 filament. As discussed in [Section 3.3](#), the IRS17 filament presents multiple velocity components, consistent with the three bundles of velocity-coherent fibers identified. The detected cores are randomly spaced in the large-scale filament. This is in good agreement with recent dynamic models using numerical simulations that consider accretion, turbulence, and magnetic fields to interpret the observed randomly-distributed core spacings ([Seifried & Walch 2015](#); [Clarke et al. 2016, 2017, 2020](#); [Gritschneider et al. 2017](#)). However, the signature of periodic core-spacing is observed in a few of the detected velocity-coherent, fertile fibers in IRS17 filament. Not consistent with the above picture of hierarchical fragmentation, are the hydrodynamical simulations by [Smith et al. \(2014, 2016\)](#). These authors propose a ‘bottom-up’ model, where fibers pre-exist in clouds, formed as a natural outcome of a turbulent cascade. Subsequently, these fibers are swept together to form the large-filaments as a consequence of the large-scale gravity-driven collapse of the cloud. The differing views advocate for further such studies of filamentary clouds at higher resolution and sensitivity for a better insight into the formation and role of fibers in star formation.

## 5. SUMMARY

We have investigated the internal structure of the IRS17 filament in the intermediate mass protocluster, IRAS 08448-4343, using both 3 mm and 1.3 mm ALMA data from the ATOMS and QUARKS survey, respectively. Our study has illustrated the role of small-scale fibers in star formation. Our major results are as follows:

A sub-parsec filament ( $\sim 0.26$  pc), referred to as the IRS17 filament, is seen in 3 mm continuum emission within the IRS17 protocluster region. The gas kinematics of this filament presents a complex and multi-component field.

Within the apparent IRS17 filament, three bundles of seven velocity-coherent fibers and twenty-nine dense condensations were revealed from the QUARKS 1.3 mm continuum map. The fibers have a median length of  $\sim 4500$  au and a median width of  $\sim 1400$  au with a line mass of  $51.9 M_{\odot} \text{ pc}^{-1}$ . We identified four fertile fibers, each hosting three or more condensations, based on the association between condensations and fibers. Some condensations are linked to ongoing star formation signatures, such as YSOs and outflows, while most are subvirial. These findings suggest that the majority of condensations could potentially seed star formation.

Furthermore, periodic spacings of condensations are observed in the fertile fibers, which agrees with linear isothermal cylinder fragmentation models. However, this periodic pattern is not observed for the detected 3 mm cores in the larger-scale IRS17 filament. This reflects the crucial role of fibers on the fragmentation of the filament into cores. In other words, there may be an intermediate fragmentation step, involving the formation of fibers, before core formation out of the IRS17 filament. This step leaves no strong imprint of quasi-periodic fragmentation of filaments into cores.

## ACKNOWLEDGEMENTS

We thank the referee for the valuable comments and suggestions that greatly improved the quality of this paper. This work has been supported by the National Key R&D Program of China (No. 2022YFA1603101). H.-L. Liu is supported by National Natural Science Foundation of China (NSFC) through the grant No.12103045, and by Yunnan Fundamental Research Project (grant No. 202301AT070118, 202401AS070121). T. Liu acknowledges the supports by NSFC through grants No.12073061 and No.12122307; and X. Liu has also been supported by CPSF No. 2022M723278; S.-L. Qin is supported by NSFC under No.12033005. G.G. gratefully acknowledges support by the ANID BASAL project FB210003. PS was partially supported by a Grant-in-Aid for Scientific Research (KAKENHI Num-

ber JP22H01271 and JP23H01221) of JSPS, and by Yoshinori Ohsumi Fund (Yoshinori Ohsumi Award for Fundamental Research). This work was performed in part at the Jet Propulsion Laboratory, California Institute of Technology, under contract with the National Aeronautics and Space Administration (80NM0018D0004). SRD acknowledges support from the Fondecyt Postdoctoral fellowship (project code

3220162) and ANID BASAL project FB210003. This work was partly supported by Yunnan Xingdian Talent Support Plan–Youth Project. LB gratefully acknowledges support by the ANID BASAL project FB210003. This paper makes use of the following ALMA data: ADS/JAO.ALMA#2019.1.00685.S, 2021.1.00095.S and 2023.1.00425.

## APPENDIX

## A. COMPLEMENTARY FIGURES AND TABLES

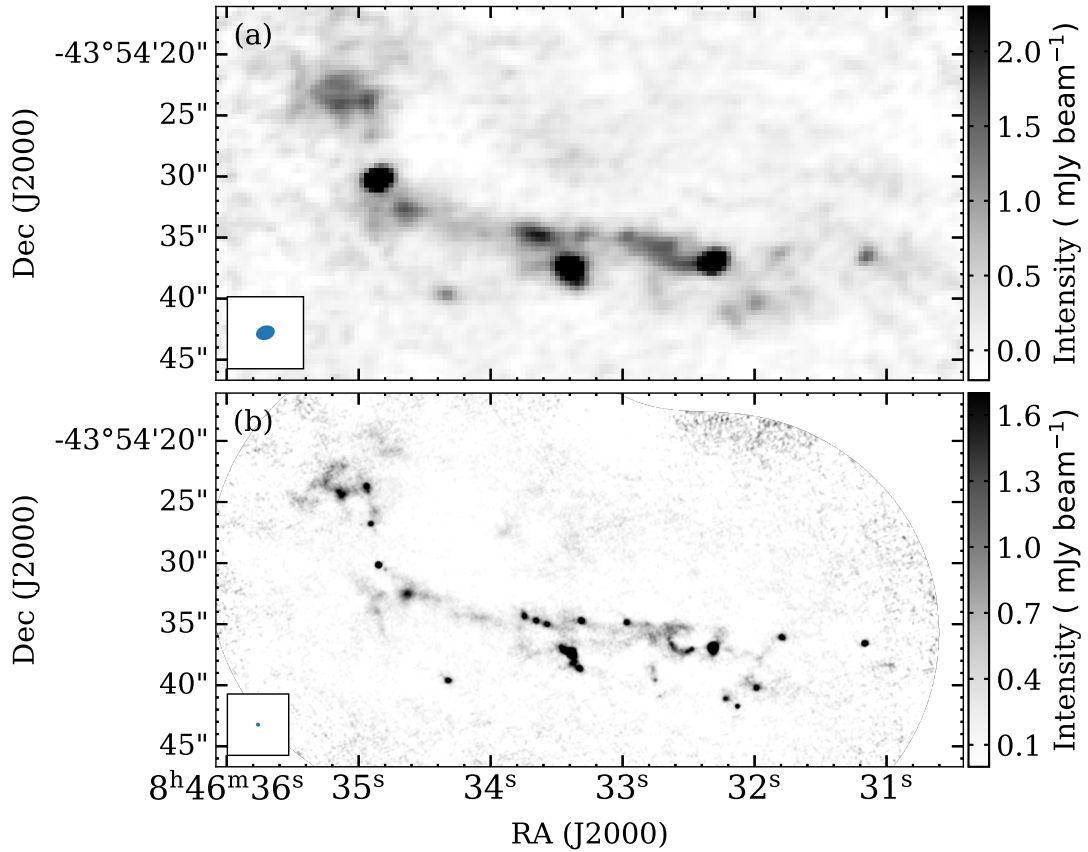


**Figure 7.** ATOMS 3-mm (panel a) and QUARKS 1.3-mm (panel b) dust continuum images without any labels.

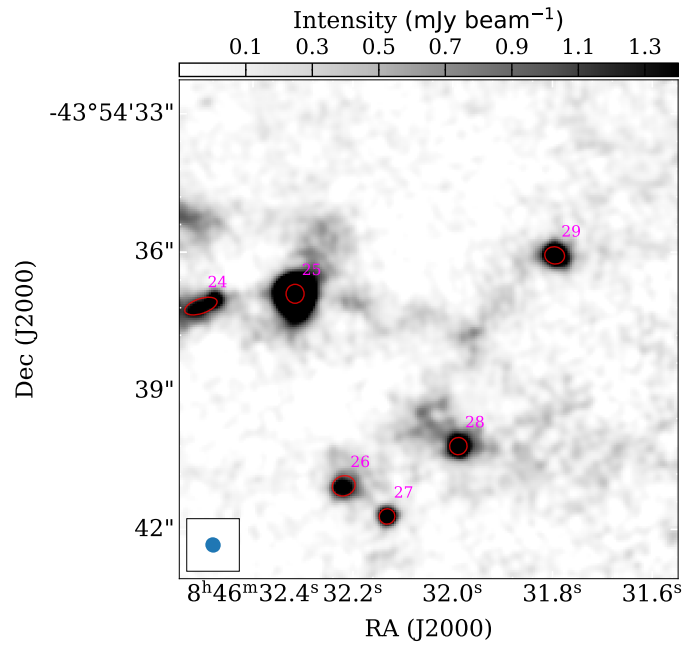


**Figure 8.** Zoomed-in map of the 1.3-mm dust continuum. A network of fibers connecting condensations 25, 28, and 29 is observable but not identified automatically by *getsf*.

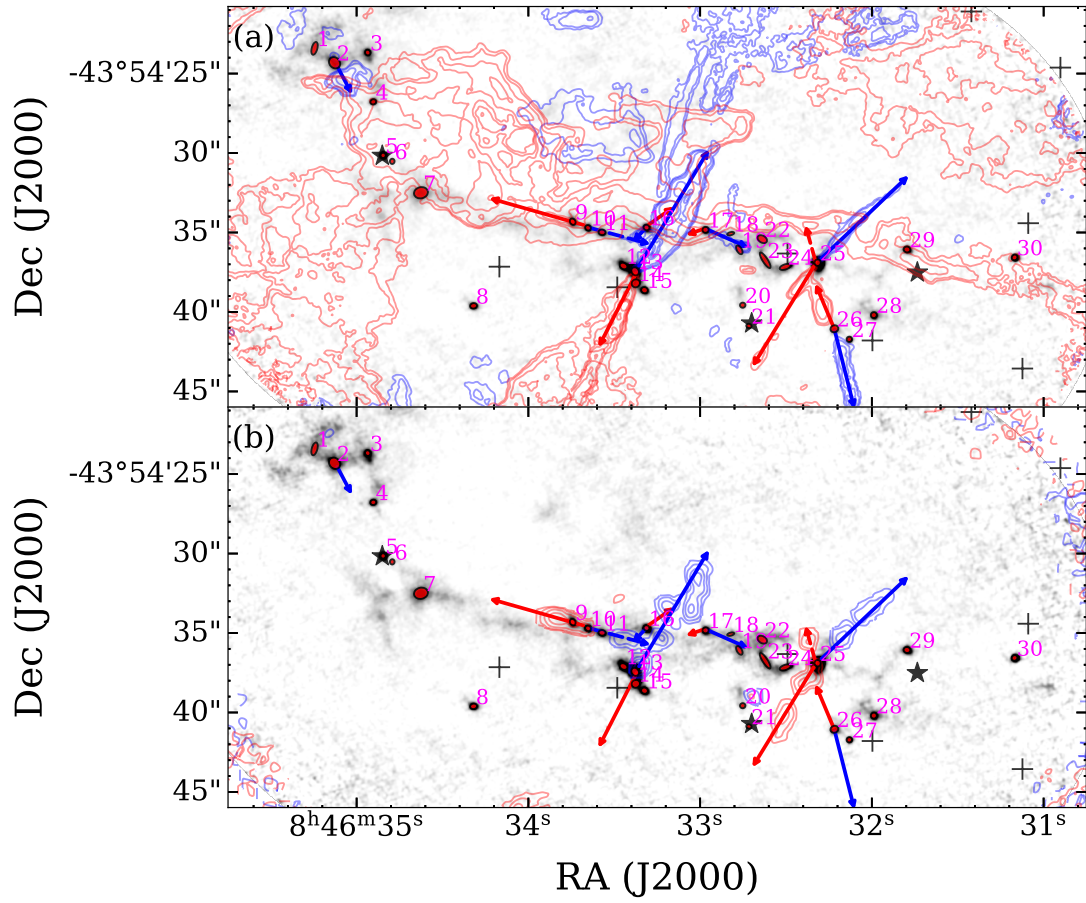


**Figure 9.** CO and SiO outflows overlaid on the 1.3 mm dust continuum. Panel (a): CO (2-1) outflows. The contours show [3, 6, 12, 24, 48]  $rms$  ( $\sim 0.04 \text{ Jy beam}^{-1} \text{ km s}^{-1}$ ). Panel (b): SiO (5-4) outflows. The contours same as panel (a), but  $rms$  of  $\sim 0.015 \text{ Jy beam}^{-1} \text{ km s}^{-1}$ .

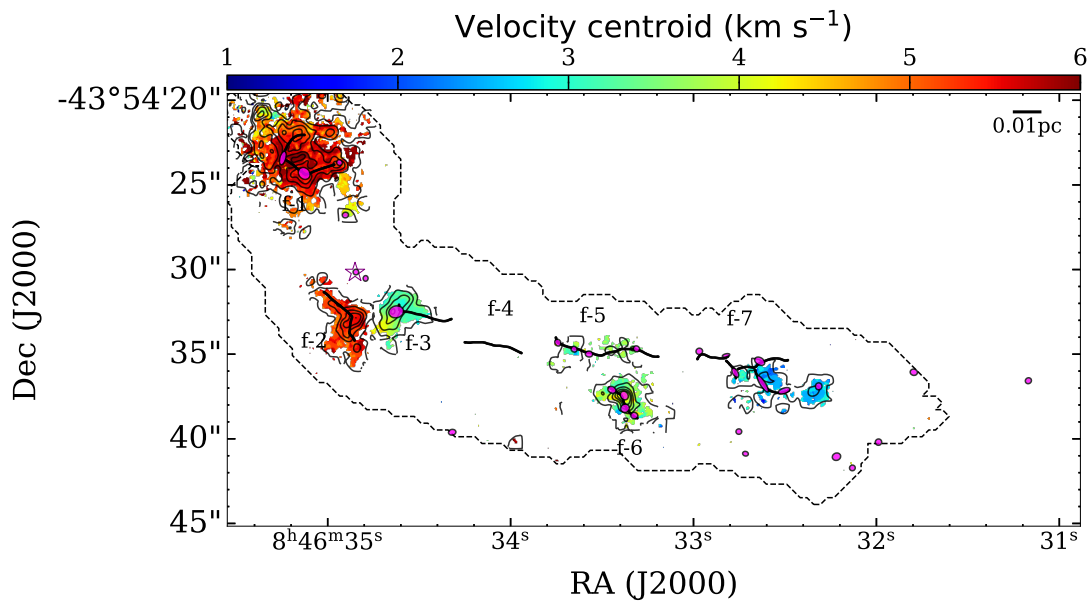


**Figure 10.** Velocity centroid (Moment 1) map of DCN line data from the QUARKS survey. The velocity range of DCN emission is set to  $[1, 6] \text{ km s}^{-1}$ . The symbol same as Fig 4, the contour levels start at  $3 \text{ rms}$  ( $\sim 0.004 \text{ Jy beam km s}^{-1}$ ), and following as  $[6, 9, 12, 15] \text{ rms}$ .

**Table 4.** Physical parameters of 1.3 mm condensations

Condensation	Position		$FWHM_{\text{maj}}$ (")	$FWHM_{\text{min}}$ (")	PA ( $^{\circ}$ )	$S_{1.3\text{mm}}^{\text{int}}$ (mJy)	$F_{1.3\text{mm}}^{\text{peak}}$ (mJy beam $^{-1}$ )	$R_c$ (au)	$M_c$ ( $M_{\odot}$ )	$n_c$ ( $\times 10^8 \text{ cm}^{-3}$ )
	$\alpha$ (J2000)	$\delta$ (J2000)								
C1*	08:46:35.24	-43:54:23.41	0.83	0.35	164.7	$3.0 \pm 0.3$	$1.2 \pm 0.1$	222.8	$0.08 \pm 0.01$	$2.19 \pm 0.35$
C2	08:46:35.13	-43:54:24.32	0.77	0.64	42.4	$6.2 \pm 0.3$	$1.3 \pm 0.2$	353.4	$0.16 \pm 0.02$	$1.1 \pm 0.18$
C3	08:46:34.94	-43:54:23.68	0.36	0.33	36.0	$4.0 \pm 0.2$	$2.9 \pm 0.2$	210.3	$0.10 \pm 0.01$	$3.26 \pm 0.52$
C4	08:46:34.90	-43:54:26.78	0.37	0.33	102.2	$3.7 \pm 0.2$	$2.8 \pm 0.2$	213.2	$0.09 \pm 0.01$	$2.81 \pm 0.44$
C5	08:46:34.85	-43:54:30.15	0.33	0.33	69.8	$11.4 \pm 0.1$	$9.4 \pm 0.1$	201.3	$0.29 \pm 0.04$	$10.76 \pm 1.71$
C6	08:46:34.79	-43:54:30.52	0.33	0.29	175.5	$0.6 \pm 0.1$	$0.6 \pm 0.1$	188.7	$0.02 \pm 0.01$	$0.90 \pm 0.18$
C7	08:46:34.63	-43:54:32.50	0.88	0.70	102.9	$6.7 \pm 0.2$	$1.1 \pm 0.1$	413.2	$0.17 \pm 0.02$	$0.73 \pm 0.08$
C8	08:46:34.32	-43:54:39.61	0.44	0.34	98.9	$6.1 \pm 0.1$	$3.2 \pm 0.1$	235.9	$0.15 \pm 0.02$	$3.46 \pm 0.44$
C9	08:46:33.74	-43:54:34.32	0.42	0.34	30.0	$4.1 \pm 0.1$	$2.4 \pm 0.1$	230.5	$0.10 \pm 0.01$	$2.47 \pm 0.39$
C10	08:46:33.65	-43:54:34.71	0.37	0.33	56.7	$4.5 \pm 0.1$	$3.1 \pm 0.1$	213.2	$0.11 \pm 0.02$	$3.44 \pm 0.55$
C11	08:46:33.57	-43:54:34.99	0.44	0.35	83.4	$3.8 \pm 0.2$	$2.1 \pm 0.2$	239.4	$0.10 \pm 0.1$	$2.21 \pm 0.35$
C12	08:46:33.45	-43:54:37.11	0.51	0.38	62.0	$7.0 \pm 0.2$	$3.5 \pm 0.2$	268.5	$0.18 \pm 0.2$	$2.82 \pm 0.45$
C13	08:46:33.38	-43:54:37.44	0.54	0.45	34.3	$19.5 \pm 0.3$	$7.7 \pm 0.3$	178.8	$0.49 \pm 0.07$	$25.95 \pm 4.13$
C14	08:46:33.37	-43:54:38.20	0.53	0.49	119.9	$4.1 \pm 0.2$	$1.7 \pm 0.2$	195.4	$0.10 \pm 0.01$	$4.06 \pm 0.59$
C15	08:46:33.32	-43:54:38.63	0.43	0.38	68.0	$6.0 \pm 0.2$	$3.4 \pm 0.2$	246.6	$0.15 \pm 0.2$	$3.03 \pm 0.48$
C16	08:46:33.31	-43:54:34.67	0.38	0.34	60.8	$6.2 \pm 0.2$	$4.2 \pm 0.2$	219.3	$0.16 \pm 0.02$	$4.59 \pm 0.73$
C17	08:46:32.97	-43:54:34.83	0.39	0.37	106.7	$4.6 \pm 0.2$	$2.9 \pm 0.2$	231.7	$0.12 \pm 0.02$	$2.92 \pm 0.46$
C18*	08:46:32.82	-43:54:35.07	0.45	0.19	103.8	$1.1 \pm 0.1$	$1.0 \pm 0.1$	178.4	$0.03 \pm 0.01$	$1.60 \pm 0.25$
C19*	08:46:32.77	-43:54:36.09	0.61	0.31	29.6	$2.8 \pm 0.3$	$1.0 \pm 0.1$	265.3	$0.07 \pm 0.01$	$1.13 \pm 0.18$
C20	08:46:32.75	-43:54:39.57	0.34	0.32	98.4	$1.1 \pm 0.2$	$0.9 \pm 0.2$	201.2	$0.03 \pm 0.01$	$1.12 \pm 0.22$
C21	08:46:32.72	-43:54:40.88	0.34	0.27	76.2	$0.8 \pm 0.1$	$0.7 \pm 0.1$	184.8	$0.02 \pm 0.01$	$0.96 \pm 0.15$
C22*	08:46:32.64	-43:54:35.42	0.64	0.43	58.7	$4.5 \pm 0.5$	$1.1 \pm 0.1$	209.6	$0.11 \pm 0.02$	$3.62 \pm 0.57$
C23*	08:46:32.62	-43:54:36.75	1.15	0.31	32.8	$6.4 \pm 0.6$	$1.7 \pm 0.2$	272.4	$0.16 \pm 0.03$	$2.40 \pm 0.38$
C24*	08:46:32.50	-43:54:37.17	0.73	0.32	108.5	$5.2 \pm 0.5$	$2.4 \pm 0.2$	294.8	$0.13 \pm 0.02$	$1.54 \pm 0.24$
C25	08:46:32.32	-43:54:36.90	0.41	0.39	179.0	$51.7 \pm 0.4$	$26.2 \pm 0.2$	243.9	$1.31 \pm 0.18$	$27.34 \pm 4.33$
C26	08:46:32.22	-43:54:41.06	0.5	0.43	109.8	$4.5 \pm 0.2$	$1.7 \pm 0.1$	282.8	$0.11 \pm 0.02$	$1.47 \pm 0.23$
C27	08:46:32.13	-43:54:41.72	0.34	0.33	121.0	$3.2 \pm 0.1$	$2.6 \pm 0.1$	204.3	$0.08 \pm 0.01$	$2.84 \pm 0.45$
C28	08:46:31.99	-43:54:40.20	0.38	0.37	119.4	$4.2 \pm 0.2$	$2.7 \pm 0.2$	228.7	$0.11 \pm 0.01$	$2.78 \pm 0.44$
C29	08:46:31.80	-43:54:36.07	0.43	0.37	77.5	$6.6 \pm 0.1$	$3.4 \pm 0.1$	243.3	$0.17 \pm 0.02$	$3.57 \pm 0.57$
C30	08:46:31.17	-43:54:36.57	0.37	0.34	124.1	$8.8 \pm 0.2$	$6.2 \pm 0.1$	216.4	$0.22 \pm 0.03$	$6.57 \pm 1.04$

\* These condensations are identified from SExtractor.

## REFERENCES

- Alves, J., Lombardi, M., & Lada, C. 2007, in *Astrophysics and Space Science Proceedings*, Vol. 3, Island Universes, 417, doi: [10.1007/978-1-4020-5573-7\\_72](https://doi.org/10.1007/978-1-4020-5573-7_72)
- André, P., Arzoumanian, D., Könyves, V., Shimajiri, Y., & Palmeirim, P. 2019, *A&A*, 629, L4, doi: [10.1051/0004-6361/201935915](https://doi.org/10.1051/0004-6361/201935915)
- André, P., Belloche, A., Motte, F., & Peretto, N. 2007, *A&A*, 472, 519, doi: [10.1051/0004-6361:20077422](https://doi.org/10.1051/0004-6361:20077422)
- André, P., Di Francesco, J., Ward-Thompson, D., et al. 2014, in *Protostars and Planets VI*, ed. H. Beuther, R. S. Klessen, C. P. Dullemond, & T. Henning, 27–51, doi: [10.2458/azu\\_uapress\\_9780816531240-ch002](https://doi.org/10.2458/azu_uapress_9780816531240-ch002)
- André, P., Men'shchikov, A., Bontemps, S., et al. 2010, *A&A*, 518, L102, doi: [10.1051/0004-6361/201014666](https://doi.org/10.1051/0004-6361/201014666)
- Arzoumanian, D., André, P., Peretto, N., & Könyves, V. 2013, *A&A*, 553, A119, doi: [10.1051/0004-6361/201220822](https://doi.org/10.1051/0004-6361/201220822)
- Arzoumanian, D., André, P., Könyves, V., et al. 2019, *A&A*, 621, A42, doi: [10.1051/0004-6361/201832725](https://doi.org/10.1051/0004-6361/201832725)
- Barbary, K. 2016, extinction v0.3.0, Zenodo, doi: [10.5281/zenodo.804967](https://doi.org/10.5281/zenodo.804967)
- Barrow, J. D., Bhavsar, S. P., & Sonoda, D. H. 1985, *MNRAS*, 216, 17, doi: [10.1093/mnras/216.1.17](https://doi.org/10.1093/mnras/216.1.17)
- Bertin, E., & Arnouts, S. 1996, *A&AS*, 117, 393, doi: [10.1051/aas:1996164](https://doi.org/10.1051/aas:1996164)
- Bertoldi, F., & McKee, C. F. 1992, *ApJ*, 395, 140, doi: [10.1086/171638](https://doi.org/10.1086/171638)
- Cao, Y., Qiu, K., Zhang, Q., & Li, G.-X. 2022, *ApJ*, 927, 106, doi: [10.3847/1538-4357/ac4696](https://doi.org/10.3847/1538-4357/ac4696)
- Chandrasekhar, S., & Fermi, E. 1953, *ApJ*, 118, 116, doi: [10.1086/145732](https://doi.org/10.1086/145732)
- Cheng, Y., Tobin, J. J., Yang, Y.-L., et al. 2022, *ApJ*, 933, 178, doi: [10.3847/1538-4357/ac7464](https://doi.org/10.3847/1538-4357/ac7464)
- Chung, E. J., Lee, C. W., Kwon, W., et al. 2023, *ApJ*, 951, 68, doi: [10.3847/1538-4357/acd540](https://doi.org/10.3847/1538-4357/acd540)
- Clarke, S. D., Whitworth, A. P., Duarte-Cabral, A., & Hubber, D. A. 2017, *MNRAS*, 468, 2489, doi: [10.1093/mnras/stx637](https://doi.org/10.1093/mnras/stx637)
- Clarke, S. D., Whitworth, A. P., & Hubber, D. A. 2016, *MNRAS*, 458, 319, doi: [10.1093/mnras/stw407](https://doi.org/10.1093/mnras/stw407)
- Clarke, S. D., Williams, G. M., & Walch, S. 2020, *MNRAS*, 497, 4390, doi: [10.1093/mnras/staa2298](https://doi.org/10.1093/mnras/staa2298)
- Contreras, Y., Schuller, F., Urquhart, J. S., et al. 2013, *A&A*, 549, A45, doi: [10.1051/0004-6361/201220155](https://doi.org/10.1051/0004-6361/201220155)
- Cox, N. L. J., Arzoumanian, D., André, P., et al. 2016, *A&A*, 590, A110, doi: [10.1051/0004-6361/201527068](https://doi.org/10.1051/0004-6361/201527068)
- Dewangan, L. K., Bhadari, N. K., Maity, A. K., et al. 2024, *MNRAS*, 527, 5895, doi: [10.1093/mnras/stad3384](https://doi.org/10.1093/mnras/stad3384)
- Dib, S., & Henning, T. 2019, *A&A*, 629, A135, doi: [10.1051/0004-6361/201834080](https://doi.org/10.1051/0004-6361/201834080)
- Faúndez, S., Bronfman, L., Garay, G., et al. 2004, *A&A*, 426, 97, doi: [10.1051/0004-6361:20035755](https://doi.org/10.1051/0004-6361:20035755)
- Fehér, O., Tóth, L. V., Ward-Thompson, D., et al. 2016, *A&A*, 590, A75, doi: [10.1051/0004-6361/201424385](https://doi.org/10.1051/0004-6361/201424385)
- Fernández-López, M., Arce, H. G., Looney, L., et al. 2014, *ApJL*, 790, L19, doi: [10.1088/2041-8205/790/2/L19](https://doi.org/10.1088/2041-8205/790/2/L19)
- Giannini, T., Massi, F., Podio, L., et al. 2005, *A&A*, 433, 941, doi: [10.1051/0004-6361:20041959](https://doi.org/10.1051/0004-6361:20041959)
- Goedhart, S., Cotton, W. D., Camilo, F., et al. 2024, *MNRAS*, 531, 649, doi: [10.1093/mnras/stae1166](https://doi.org/10.1093/mnras/stae1166)
- Gritschneider, M., Heigl, S., & Burkert, A. 2017, *ApJ*, 834, 202, doi: [10.3847/1538-4357/834/2/202](https://doi.org/10.3847/1538-4357/834/2/202)
- Hacar, A., Clark, S. E., Heitsch, F., et al. 2023, in *Astronomical Society of the Pacific Conference Series*, Vol. 534, *Protostars and Planets VII*, ed. S. Inutsuka, Y. Aikawa, T. Muto, K. Tomida, & M. Tamura, 153, doi: [10.48550/arXiv.2203.09562](https://doi.org/10.48550/arXiv.2203.09562)
- Hacar, A., Tafalla, M., & Alves, J. 2017, *A&A*, 606, A123, doi: [10.1051/0004-6361/201630348](https://doi.org/10.1051/0004-6361/201630348)
- Hacar, A., Tafalla, M., Forbrich, J., et al. 2018, *A&A*, 610, A77, doi: [10.1051/0004-6361/201731894](https://doi.org/10.1051/0004-6361/201731894)
- Hacar, A., Tafalla, M., Kauffmann, J., & Kovács, A. 2013, *A&A*, 554, A55, doi: [10.1051/0004-6361/201220090](https://doi.org/10.1051/0004-6361/201220090)
- Inutsuka, S.-I., & Miyama, S. M. 1992, *ApJ*, 388, 392, doi: [10.1086/171162](https://doi.org/10.1086/171162)
- Jackson, J. M., Finn, S. C., Chambers, E. T., Rathborne, J. M., & Simon, R. 2010, *ApJL*, 719, L185, doi: [10.1088/2041-8205/719/2/L185](https://doi.org/10.1088/2041-8205/719/2/L185)
- Kainulainen, J., Stutz, A. M., Stanke, T., et al. 2017, *A&A*, 600, A141, doi: [10.1051/0004-6361/201628481](https://doi.org/10.1051/0004-6361/201628481)
- Könyves, V., André, P., Men'shchikov, A., et al. 2010, *A&A*, 518, L106, doi: [10.1051/0004-6361/201014689](https://doi.org/10.1051/0004-6361/201014689)
- Könyves, V., André, P., Arzoumanian, D., et al. 2020, *A&A*, 635, A34, doi: [10.1051/0004-6361/201834753](https://doi.org/10.1051/0004-6361/201834753)
- Larson, R. B. 1981, *MNRAS*, 194, 809, doi: [10.1093/mnras/194.4.809](https://doi.org/10.1093/mnras/194.4.809)
- Li, S., Sanhueza, P., Lee, C. W., et al. 2022, *ApJ*, 926, 165, doi: [10.3847/1538-4357/ac3df8](https://doi.org/10.3847/1538-4357/ac3df8)
- Liseau, R., Lorenzetti, D., Nisini, B., Spinoglio, L., & Moneti, A. 1992, *A&A*, 265, 577
- Liu, H.-L., Stutz, A., & Yuan, J.-H. 2018, *MNRAS*, 478, 2119, doi: [10.1093/mnras/sty1270](https://doi.org/10.1093/mnras/sty1270)
- . 2019, *MNRAS*, 487, 1259, doi: [10.1093/mnras/stz1340](https://doi.org/10.1093/mnras/stz1340)
- Liu, H.-L., Liu, T., Evans, Neal J., I., et al. 2021, *MNRAS*, 505, 2801, doi: [10.1093/mnras/stab1352](https://doi.org/10.1093/mnras/stab1352)
- Liu, H.-L., Tej, A., Liu, T., et al. 2022a, *MNRAS*, 510, 5009, doi: [10.1093/mnras/stab2757](https://doi.org/10.1093/mnras/stab2757)

- . 2022b, MNRAS, 511, 4480, doi: [10.1093/mnras/stac378](https://doi.org/10.1093/mnras/stac378)
- . 2023, MNRAS, 522, 3719, doi: [10.1093/mnras/stad047](https://doi.org/10.1093/mnras/stad047)
- Liu, T., Evans, N. J., Kim, K.-T., et al. 2020a, MNRAS, 496, 2790, doi: [10.1093/mnras/staa1577](https://doi.org/10.1093/mnras/staa1577)
- . 2020b, MNRAS, 496, 2821, doi: [10.1093/mnras/staa1501](https://doi.org/10.1093/mnras/staa1501)
- Liu, X., Liu, T., Zhu, L., et al. 2024, Research in Astronomy and Astrophysics, 24, 025009, doi: [10.1088/1674-4527/ad0d5c](https://doi.org/10.1088/1674-4527/ad0d5c)
- Lorenzetti, D., Giannini, T., Vitali, F., Massi, F., & Nisini, B. 2002, ApJ, 564, 839, doi: [10.1086/324305](https://doi.org/10.1086/324305)
- Louvet, F., Sanhueza, P., Stutz, A., et al. 2024, arXiv e-prints, arXiv:2407.18719, doi: [10.48550/arXiv.2407.18719](https://doi.org/10.48550/arXiv.2407.18719)
- Lu, X., Zhang, Q., Liu, H. B., Wang, J., & Gu, Q. 2014, ApJ, 790, 84, doi: [10.1088/0004-637X/790/2/84](https://doi.org/10.1088/0004-637X/790/2/84)
- Luo, A.-X., Liu, H.-L., Qin, S.-L., Yang, D.-t., & Pan, S. 2024, AJ, 167, 228, doi: [10.3847/1538-3881/ad35ca](https://doi.org/10.3847/1538-3881/ad35ca)
- Mai, X., Liu, T., Liu, X., et al. 2024, ApJL, 961, L35, doi: [10.3847/2041-8213/ad19c3](https://doi.org/10.3847/2041-8213/ad19c3)
- Massi, F., Giannini, T., Lorenzetti, D., et al. 1999, A&AS, 136, 471, doi: [10.1051/aas:1999471](https://doi.org/10.1051/aas:1999471)
- McMullin, J. P., Waters, B., Schiebel, D., Young, W., & Golap, K. 2007, in Astronomical Society of the Pacific Conference Series, Vol. 376, Astronomical Data Analysis Software and Systems XVI, ed. R. A. Shaw, F. Hill, & D. J. Bell, 127
- Men'shchikov, A. 2021, A&A, 649, A89, doi: [10.1051/0004-6361/202039913](https://doi.org/10.1051/0004-6361/202039913)
- Molinari, S., Swinyard, B., Bally, J., et al. 2010, A&A, 518, L100, doi: [10.1051/0004-6361/201014659](https://doi.org/10.1051/0004-6361/201014659)
- Motte, F., André, P., & Neri, R. 1998, A&A, 336, 150
- Motte, F., Bontemps, S., & Louvet, F. 2018, ARA&A, 56, 41, doi: [10.1146/annurev-astro-091916-055235](https://doi.org/10.1146/annurev-astro-091916-055235)
- Mottram, J. C., Hoare, M. G., Lumsden, S. L., et al. 2007, A&A, 476, 1019, doi: [10.1051/0004-6361:20077663](https://doi.org/10.1051/0004-6361:20077663)
- Murphy, D. C., & May, J. 1991, A&A, 247, 202
- Nagasawa, M. 1987, Progress of Theoretical Physics, 77, 635, doi: [10.1143/PTP.77.635](https://doi.org/10.1143/PTP.77.635)
- Ohashi, S., Sanhueza, P., Sakai, N., et al. 2018, ApJ, 856, 147, doi: [10.3847/1538-4357/aab3d0](https://doi.org/10.3847/1538-4357/aab3d0)
- Ossenkopf, V., & Henning, T. 1994, A&A, 291, 943
- Ostriker, J. 1964, ApJ, 140, 1056, doi: [10.1086/148005](https://doi.org/10.1086/148005)
- Padmanabh, P. V., Barr, E. D., Sridhar, S. S., et al. 2023, MNRAS, 524, 1291, doi: [10.1093/mnras/stad1900](https://doi.org/10.1093/mnras/stad1900)
- Padoan, P., Pan, L., Juvela, M., Haugbølle, T., & Nordlund, Å. 2020, ApJ, 900, 82, doi: [10.3847/1538-4357/abaa47](https://doi.org/10.3847/1538-4357/abaa47)
- Palmeirim, P., André, P., Kirk, J., et al. 2013, A&A, 550, A38, doi: [10.1051/0004-6361/201220500](https://doi.org/10.1051/0004-6361/201220500)
- Pouteau, Y., Motte, F., Nony, T., et al. 2022, A&A, 664, A26, doi: [10.1051/0004-6361/202142951](https://doi.org/10.1051/0004-6361/202142951)
- . 2023, A&A, 674, A76, doi: [10.1051/0004-6361/202244776](https://doi.org/10.1051/0004-6361/202244776)
- Sanhueza, P., Jackson, J. M., Foster, J. B., et al. 2012, ApJ, 756, 60, doi: [10.1088/0004-637X/756/1/60](https://doi.org/10.1088/0004-637X/756/1/60)
- Sanhueza, P., Contreras, Y., Wu, B., et al. 2019, ApJ, 886, 102, doi: [10.3847/1538-4357/ab45e9](https://doi.org/10.3847/1538-4357/ab45e9)
- Seifried, D., & Walch, S. 2015, MNRAS, 452, 2410, doi: [10.1093/mnras/stv1458](https://doi.org/10.1093/mnras/stv1458)
- Shimajiri, Y., André, P., Palmeirim, P., et al. 2019, A&A, 623, A16, doi: [10.1051/0004-6361/201834399](https://doi.org/10.1051/0004-6361/201834399)
- Shimajiri, Y., André, P., Peretto, N., et al. 2023, A&A, 672, A133, doi: [10.1051/0004-6361/202140857](https://doi.org/10.1051/0004-6361/202140857)
- Smith, R. J., Glover, S. C. O., & Klessen, R. S. 2014, MNRAS, 445, 2900, doi: [10.1093/mnras/stu1915](https://doi.org/10.1093/mnras/stu1915)
- Smith, R. J., Glover, S. C. O., Klessen, R. S., & Fuller, G. A. 2016, MNRAS, 455, 3640, doi: [10.1093/mnras/stv2559](https://doi.org/10.1093/mnras/stv2559)
- Stodólkiewicz, J. S. 1963, Acta Astronomica, 13, 30
- Strafella, F., Elia, D., Campeggio, L., et al. 2010, ApJ, 719, 9, doi: [10.1088/0004-637X/719/1/9](https://doi.org/10.1088/0004-637X/719/1/9)
- Strafella, F., Lorenzetti, D., Giannini, T., et al. 2015, ApJ, 798, 104, doi: [10.1088/0004-637X/798/2/104](https://doi.org/10.1088/0004-637X/798/2/104)
- Stutz, A. M., & Gould, A. 2016, A&A, 590, A2, doi: [10.1051/0004-6361/201527979](https://doi.org/10.1051/0004-6361/201527979)
- Tafalla, M., & Hacar, A. 2015, A&A, 574, A104, doi: [10.1051/0004-6361/201424576](https://doi.org/10.1051/0004-6361/201424576)
- Treviño-Morales, S. P., Fuente, A., Sánchez-Monge, Á., et al. 2019, A&A, 629, A81, doi: [10.1051/0004-6361/201935260](https://doi.org/10.1051/0004-6361/201935260)
- Urquhart, J. S., Csengeri, T., Wyrowski, F., et al. 2014, A&A, 568, A41, doi: [10.1051/0004-6361/201424126](https://doi.org/10.1051/0004-6361/201424126)
- Vázquez-Semadeni, E., Palau, A., Ballesteros-Paredes, J., Gómez, G. C., & Zamora-Avilés, M. 2019, MNRAS, 490, 3061, doi: [10.1093/mnras/stz2736](https://doi.org/10.1093/mnras/stz2736)
- Wang, K., Testi, L., Burkert, A., et al. 2016, ApJS, 226, 9, doi: [10.3847/0067-0049/226/1/9](https://doi.org/10.3847/0067-0049/226/1/9)
- Xu, F., Wang, K., Liu, T., et al. 2024a, arXiv e-prints, arXiv:2404.02275, doi: [10.48550/arXiv.2404.02275](https://doi.org/10.48550/arXiv.2404.02275)
- . 2024b, ApJS, 270, 9, doi: [10.3847/1538-4365/acfee5](https://doi.org/10.3847/1538-4365/acfee5)
- Xu, F.-W., Wang, K., Liu, T., et al. 2023, MNRAS, 520, 3259, doi: [10.1093/mnras/stad012](https://doi.org/10.1093/mnras/stad012)
- Yoo, H., Lee, C. W., Chung, E. J., et al. 2023, ApJ, 957, 94, doi: [10.3847/1538-4357/acf8c2](https://doi.org/10.3847/1538-4357/acf8c2)
- Zhang, G.-Y., André, P., Men'shchikov, A., & Wang, K. 2020, A&A, 642, A76, doi: [10.1051/0004-6361/202037721](https://doi.org/10.1051/0004-6361/202037721)
- Zhang, Q., Wang, K., Lu, X., & Jiménez-Serra, I. 2015, ApJ, 804, 141, doi: [10.1088/0004-637X/804/2/141](https://doi.org/10.1088/0004-637X/804/2/141)